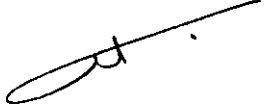


***Numerical Modeling of Impinging Jets
using various Turbulence Models***

by
Abdalla Mohammad Jawdat

Supervisor
Professor Bassam Ali Jubran

عميد كلية الدراسات العليا


**Submitted in Partial Fulfillment of the Requirements for the
Degree of Master of Science in
Mechanical Engineering**

**Faculty of Graduate Studies
University of Jordan**

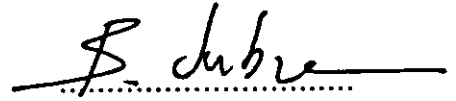
December 1996

This thesis was successfully defended and approved on 29/12/1996.

Examination Committee

Signature

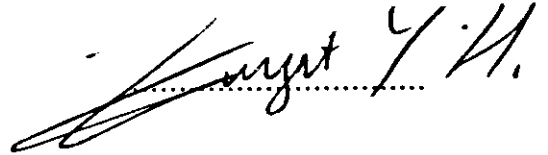
Prof. Bassam Ali Jubran, Chairman



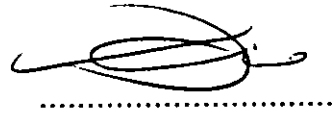
Dr. Saad Al-Habali, Member



Dr. Yousif Zurigat, Member



Dr. Mohammad Amr, Member



ACKNOWLEDGEMENTS

The author is deeply grateful to his supervisor Professor Bassam Ali Jubran for his help, guidance, and encouragement throughout the work of this thesis. Thanks are also due to Professor Radwan Shaban, Engineer Baha Suleiman, and Engineer Amr Yasin for their valuable assistance. Also, worthy of mention is the computer lab staff of the Faculty of Engineering and Technology for their support regarding the computer facilities. Not to forget all the author's colleagues and friends who were interested in this work.

Special thanks are indebted to the author's father and all his family members for their great encouragement, advice, and support. Finally, a word of thanks is due to the author's wife for her help, care, and sharing.

List of Contents

Committee decision	II
Acknowledgements	III
List of Contents	IV
List of Tables	VII
List of Figures	VIII
Nomenclature	X
Abstract	XIII
Chapter 1	
Introduction	1
1.1 Introduction	1
1.2 The Flow Field	1
1.2.1 The Free Jet Region	2
1.2.2 The Impingement Region	2
1.2.3 The Wall Jet Region	3
1.3 Turbulence Modeling	4
1.3.1 Zero-equation models	5
1.3.2 One-equation models	5
1.3.3 Two-equation models	6
1.3.4 Reynolds Stress equation models	6
1.3.5 Two-layer models	7
1.4 Thesis Objective And Layout	8
Chapter 2	
Literature Survey	11
2.1 Introduction	11
2.2 Experimental Investigation	11

2.3 Numerical Investigation	18
Chapter 3	
Mathematical Modeling	23
3.1 Introduction	23
3.2 Governing Equations	24
3.3 Grid Layout	30
3.4 Derivation of Discretized Equations	31
3.5 Treatment of Velocity-Pressure Coupling	33
3.6 Boundary Conditions	33
3.6.1 Fluid entry plane	34
3.6.2 Fluid exit plane	34
3.6.3 Axis of symmetry	34
3.6.4 Entrainment boundary	35
3.6.5 Wall boundary	35
3.7 Sequence of Solution Steps	36
3.8 Solution Procedure	37
3.8.1 Convergence criterion	37
3.8.2 Under-relaxation	38
3.8.3 Multi-grid technique	38
3.8.4 Solution strategy	39
Chapter 4	
Results and Discussions	43
4.1 Introduction	43
4.2 k- ϵ model results	46
4.2.1 Jet spreading rate	46
4.2.2 Maximum velocity decay	47

4.3 Algebraic stress model results	47
4.3.1 Jet spreading rate	47
4.3.2 Maximum velocity decay	48
4.4 Two-layer model results	48
4.4.1 Jet spreading rate	48
4.4.2 Maximum velocity decay	49
4.5 Turbulence models comparisons	49
Chapter 5	
Conclusions and Recommendations	62
5.1 Introduction	62
5.2 Conclusions	62
5.3 Recommendations	63
References	65
Appendix A	
Algebraic Reynolds Stresses Equations	69
Abstract in Arabic	

List of Tables

Table 3.1: Exchange coefficients and sources.	26
Table 3.2: Standard k- ϵ turbulence model's constants.	27
Table 3.3: Algebraic stress model constants.	30
Table 4.1: The parameters of the tested cases.	44
Table 4.2: Comparisons of the slope of the wall jet thickness curves.	44

List of Figures

Figure 1.1: The turbulent impinging jet.	9
Figure 1.2: Classification of turbulence models.	10
Figure 3.1: Grid layout and control volumes and surfaces.	40
Figure 3.2: Flow diagrams for SIMPLE and PISO.	41
Figure 3.3: Boundary conditions for the impinging jet problem.	42
Figure 4.1: Comparison between Bray's results and present results using k- ϵ model and same grid specification.	51
Figure 4.2: Grid independancy test for case 2.	51
Figure 4.3: Wall jet spreading with r/h for k- ϵ model: case 1.	52
Figure 4.4: Wall jet spreading with r/h for k- ϵ model: case 2.	52
Figure 4.5: Wall jet spreading with r/d for k- ϵ model: case 2.	53
Figure 4.6: Wall jet velocity decay against r/h for k- ϵ model: case 1.	53
Figure 4.7: Wall jet velocity decay against r/h for k- ϵ model: case 2.	54
Figure 4.8: Wall jet spreading against r/h for ASM: case 1.	54
Figure 4.9: Wall jet spreading against r/h for ASM: case 2.	55
Figure 4.10: Wall jet spreading against r/d for ASM: case 2.	55
Figure 4.11: Wall jet velocity decay against r/h for ASM: case 1.	56
Figure 4.12: Wall jet velocity decay against r/h for ASM: case 2.	56
Figure 4.13: Wall jet spreading against r/h for two-layer model: case 1.	57
Figure 4.14: Wall jet spreading against r/h for two-layer model: case 2.	57
Figure 4.15: Wall jet spreading against r/d for two-layer model: case 2.	58
Figure 4.16: Wall jet velocity decay against r/h for two-layer model: case 1.	58

Figure 4.17: Wall jet velocity decay against r/h for two-layer model: case 2.	59
Figure 4.18: Wall jet spreading against r/h for the three models: case 1.	59
Figure 4.19: Wall jet spreading against r/h for the three models: case 2.	60
Figure 4.20: Wall jet spreading against r/d for the three models: case 2.	60
Figure 4.21: Wall jet velocity decay against r/h for the three models: case 1.	61
Figure 4.22: Wall jet velocity decay against r/h for the three models: case 2.	61

Nomenclature

Abbreviations

ADI	Alternating Direction Implicit
ASM	Algebraic Stress Model
ASTOVL	Advanced Short Take-Off and Vertical Landing
CFD	Computational Fluid Dynamics
PISO	Pressure Implicit Solution by Split Operator
PLDS	Power Law Differencing Scheme
QUICK	Quadratic Upstream-Weighted Differencing Scheme
SIMPLE	Semi Implicit Method for Pressure Linked Equations
SOR	Successive Over Relaxation
STOVL	Short Take-Off and Vertical Landing
TDMA	Tri-Diagonal Matrix Algorithm
VTOL	Vertical Take-Off and Landing

Symbols

$a's$	combined diffusion and convection numerical coefficient
a_w	wall jet thickness
d	diameter
E	roughness factor for a smooth wall
G	production of turbulent kinetic energy
h	height of the nozzle above the ground
k	turbulent kinetic energy
KM	kinematic momentum flux of jet at nozzle exit

l_m , and l	turbulent length scales
p	pressure
P_m	nozzle pressure ratio
P_{ij}	production of algebraic stresses
S_ϕ	Source of the scalar quantity ϕ
U	x-axis mean velocity
u	x-axis instantaneous velocity
V	radial mean velocity
v	radial instantaneous velocity
x	axial distance
r	radial distance
TI	turbulence intensity
y^+	dimensionless wall distance

also \overline{uu} , \overline{uv} , and \overline{vv} are the Reynolds stresses and C_1 , C_2 , C_μ , C_D , C_s , and C_{sl} are turbulence models constants.

Greek symbols

ε	dissipation of turbulent kinetic energy
ϕ	general variable ($\phi= U, V, k$, or ε)
γ	algebraic stress model constant
ρ	density
τ	shear stress
μ_l	laminar viscosity
μ_t	turbulent viscosity
μ_{eff}	effective viscosity
ν	kinematic viscosity

σ_k , and σ_ϵ	standard k- ϵ model constants
Γ^ϕ	exchange coefficients for variable ϕ
κ	Von Karman's constant
$\delta_{i,j}$	Kronecker delta

Common Subscripts

in	inflow (jet exit) properties
m	maximum
n	nozzle properties
w	wall

Abstract

Numerical Modeling of Impinging Jets using various Turbulence Models

by

Abdalla M. Jawdat

Supervisor

Prof. Bassam Ali Jubran

In this study, the flow field of an incompressible turbulent impinging jet was predicted numerically using three different turbulence models. These models are the $k-\epsilon$ model, the two-layer model, and the algebraic stress model. Two different impinging cases were studied and their results were compared to previous experimental and computational results.

The investigations showed that the algebraic stress model results were a little better than those of the other two models in terms of the wall jet thickness and its spreading rate. The $k-\epsilon$ model was found to give very good results when used with proper boundary conditions and grid resolution and distribution. The two-layer model results in good prediction for the maximum velocity decay for fine grids. The multi grid technique was found to be superior in improving convergence and hence, reducing computational effort and time.

Chapter 1

Introduction

1.1 Introduction

The importance of the turbulent impinging jets on a flat plate is due to two reasons. First, they appear in various applications, such as spraying, heat transfer in many industrial processes concerned with cooling and heating, flow field around Short Take-Off and Vertical Landing Aircraft (STOVL), etc. The second reason is that they are a good test case for general (universal) turbulence models because they contain both the near wall and the free shear layers interacting with each other.

1.2 The Flow Field

The flow field of an impinging jet on a flat plate can be divided into three main regions of different characteristics although they are not independent. These regions are : the free jet region, the impingement region, and the wall jet region (Donaldson and Snedeker, 1971) and they are illustrated schematically in Figure 1.1.

1.2.1 The Free Jet Region

The free jet region is that part of the impinging jet found upstream of any strong local interaction effects due to impingement. The flow characteristics are identical to those of the free jet issuing into still conditions (Beltaos and Rajaratnam, 1977). It has a potential core with a maximum velocity surrounded by a shear layer in which the velocity drops to zero at its outer edge. This potential core extends to approximately six diameters downstream (Nosseir, 1986), beyond which the mean velocity profiles approach the self-similarity shape. The maximum velocity at the jet center line decays with vertical distance as the mixing region spreads out due to entrainment.

1.2.2 The Impingement Region

This region extends upstream of the flat plate to a location where the mean properties of the flow deviate by 2% from that value the free jet would have had at the same location (Nosseir, 1986). It has a nearly hemispherical form through which the jet undergoes considerable deflection from quasi-perpendicular to quasi-parallel to the flat plate (Araujo *et al.*, 1982). In this relatively small region, the static pressure varies from a maximum value at the center, which can be assumed to be equal to the value of the jet's total

pressure before impingement, to the ambient value at the boundary (Bray, 1991). The flow can be considered to act in an inviscid manner since it is so dominated by the pressure gradients.

1.2.3 The Wall Jet Region

The jet becomes almost parallel to the flat plate forming a flow pattern similar to that of a radial wall jet where the effects of interaction due to the impingement are no longer important (Araujo *et al.*, 1982). Two separate layers can be identified in this region, the wall layer where the frictional effects are significant and an outer free shear layer which is characterized by the features of a free turbulent jet. The maximum velocity parallel to the wall decays downstream due to the effect of entrainment and turbulent mixing. It is found that the rate of jet spreading of the wall jet is less than that of the free jet (Malin, 1989). This reduction in the spreading rates mainly appeared to be due to the damping of lateral velocity fluctuation by the wall and not only to the action of the wall shear stress on the flow (Ljuboja and Rodi, 1980).

1.3 Turbulence Modeling

The time averaging of the instantaneous quantities in the Navier-Stokes equations which describe a turbulent motion results in more unknowns which are called the Reynolds Stresses. As a consequence the equations of the turbulent motion are outnumbered and the system has to be closed. This familiar "Closure" problem is solved by what are called "Turbulence Models" which imply assumptions and correlations that enable the equality of the number of equations and the number of unknowns.

The turbulence models are placed in two categories, namely the first order and second order models (Arpaci and Larsen, 1984). The Reynolds stresses in the first order category are prescribed using the Boussinesq' or the eddy-viscosity concept. This concept assumes that, in analogy to the viscous stresses in laminar flows, the Reynolds stresses are proportional to the mean-velocity gradients (Rodi, 1980). In the second order models, the Reynolds stresses are expressed by either differential or algebraic equations. The turbulence models are also classified based on the number of transport equations solved in addition to the mean flow equations (Nallasamy, 1987):

- zero-equation models,
- one-equation models,
- two-equation models, and

- multi- (or stress) equation models.

The classification of the turbulence models is illustrated in Figure 1.2.

1.3.1 Zero-equation models

Zero-equation models are based on the Prandtl's mixing length hypothesis which calculates the distribution of eddy viscosity by relating it to the mean velocity gradient :

$$\nu_t = C_\mu l_m^2 \left| \frac{\partial U}{\partial y} \right| \quad (1.1)$$

Although these models are easy to implement in computer codes and computationally economical, they are unsuitable for complex flows because it is very difficult to estimate the distribution of the mixing length (l_m).

1.3.2 One-equation models

The one-equation model solves for a transport equation for the turbulent kinetic energy k . This transport equation is derived from the Navier-Stokes equation. The eddy viscosity is then calculated by:

$$\nu_t = C_\mu k^{\frac{1}{2}} l \quad (1.2)$$

where (l) is a flow dependent length scale which is specified algebraically, therefore it is difficult to be determined for complex flows with separation, streamline curvature, or rotation.

these models need very high computational efforts, some model approximations are introduced reducing the differential equations of the Reynolds stresses to algebraic equations (Rodi, 1976).

1.3.5 Two-layer models

The main idea of the two-layer models is to solve the turbulent problem with a certain turbulence model in the bulk of the flow not too close to the wall and resolve the viscosity affected near-wall layer with a simpler model. These two models have to be matched at some location near the edge of the viscous sublayer (Rodi, 1991).

1.4 Thesis objective and layout

The objective of this thesis is to predict the flow field of a incompressible turbulent impinging jet using several turbulence models namely: the standard k - ϵ model, the algebraic stress model, and the two-layer model. A comparison with previous experimental and numerical results will be presented to highlight the suitability of these turbulence models to predict such a phenomenon.

The thesis consists of five chapters, of which this introduction is the first. Chapter 2 is a literature review of previous experimental and numerical work related to the problem. Chapter 3 describes the mathematical modeling of the problem and the computer code used to solve it numerically along with details of the used turbulence models. Chapter 4 includes the presentation and the discussion of the predicted results. Finally, chapter 5 reports the conclusions gained from the present investigation, followed by recommendations for future work.

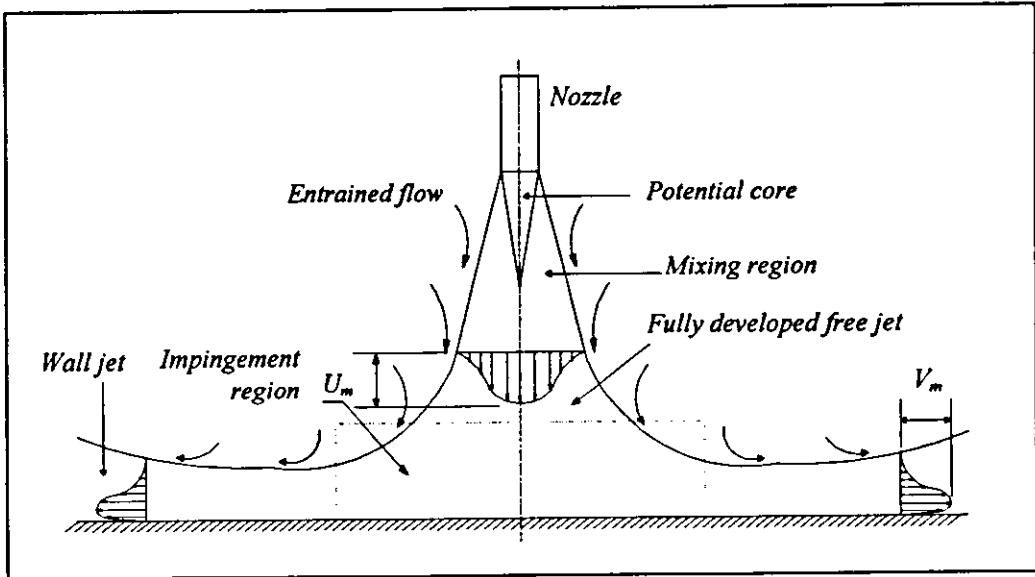


Figure 1.1: The turbulent impinging jet.

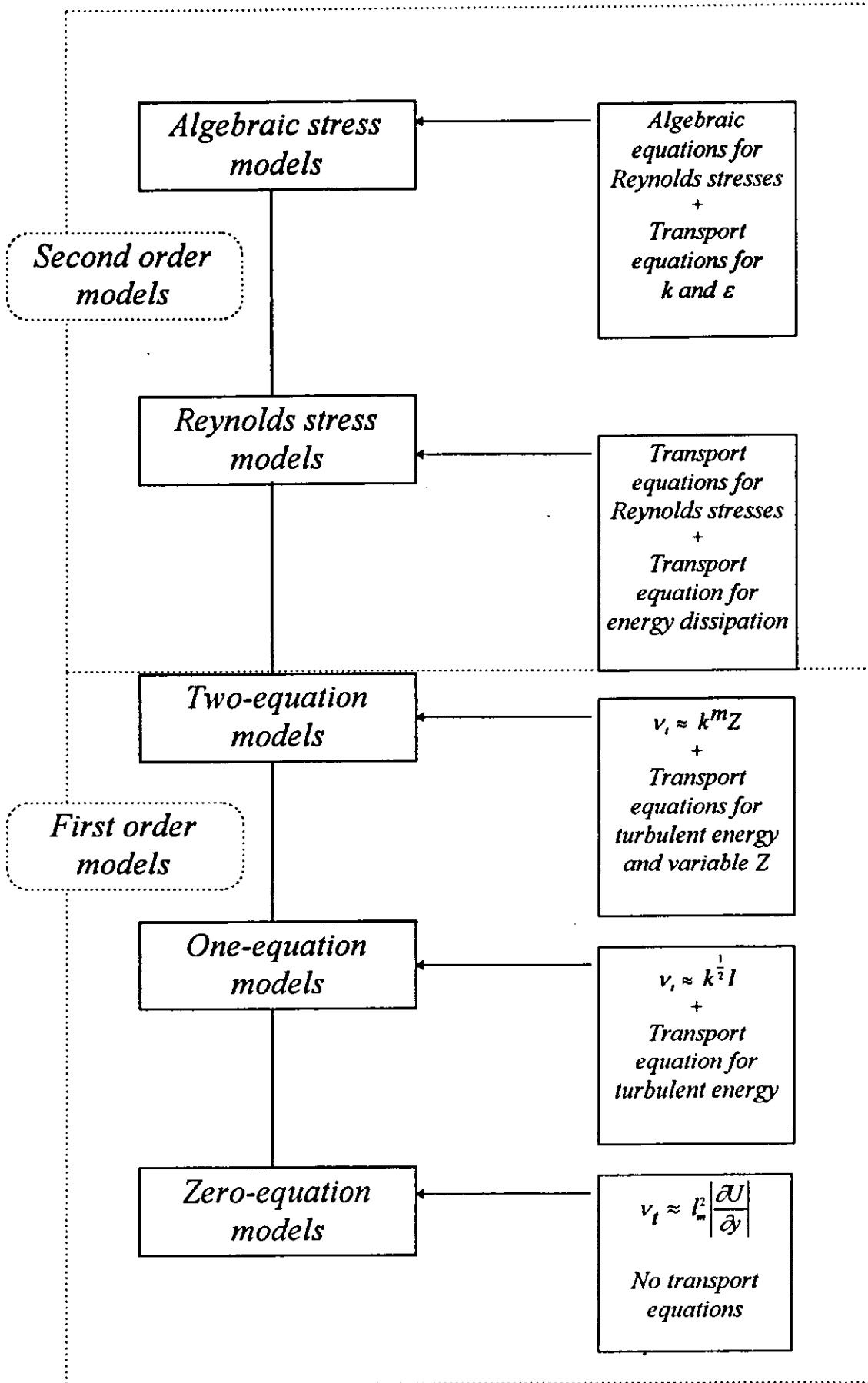


Figure 1.2: Classification of turbulence models.

Chapter 2

Literature Survey

2.1 Introduction

Numerous experimental and numerical investigations were performed in the last three decades concerning free, wall, and impinging jets. Most of the previous numerical investigations had used the well known $k-\epsilon$ turbulence model. This work is dedicated to the numerical modeling of a single incompressible impinging jet without cross flow using the $k-\epsilon$ model along with other turbulence models. Hence, the literature survey will include a review on the experimental and numerical investigations of the impinging jets without cross flow in order to provide a better understanding of our problem and to compare the present work with them.

476770

2.2 Experimental Investigations

Brady and Ludwig (1963) studied the flow processes in a uniform impinging jet. Data were obtained at five ground board locations and two jet nozzle velocities. The nondimensionalized pressure distributions on the

ground board, which was found to be independent of the jet velocity, and along the jet centerline were plotted. The nondimensionalized velocity profiles were identical for nozzle height to nozzle diameter ratio greater than 1.0 within the experimental error. Plots for tangential velocities versus the wall jet half width were also presented.

Poreh *et al.* (1967) studied six test impinging jet conditions with fixed height and various orifice diameters and exit velocities. They used hot wire anemometer to obtain the wall jet data and dimensional analysis to show the effect of initial jet characteristics on the wall jet. They showed that the flow field of the wall jet is dependent on the jet height even at large radial distance from the stagnation point. The velocity field of the wall jet was found to be approximately similar and slightly dependent on the overall Reynolds number of the flow. It was also found that the rate of spread of the jet is smaller, and the rate of decay of the radial velocities is larger than those of a free jet. Furthermore, their wall jet velocity profiles agree well with the analytical work of Glauert (1956) although the data do not confirm some of Glauert's assumptions. Poreh *et al.* showed that the shear stress does not vanish at the zero velocity-gradient point. The measurements of turbulent intensities indicated that the turbulent level in the wall jet is higher than in boundary layers and pipe flow. Finally, the measurements of the Reynolds stresses indicated that the turbulent shear stress is not proportional

to the local gradient of the mean velocities as assumed by the eddy-viscosity model.

Donaldson and Snedeker (1971) studied experimentally the behaviour of normal and oblique impinging jets for different parameters, namely: mass flow rate, height of the nozzle, angle of impinging, and impingement surface shape. For the normal impinging case, which is the area of interest in this work, they plotted the distribution of the nondimensionalized pressure against the radial distance from the stagnation point. They compared these distributions with those of the free jet and found that they are similar in the general local character though there is a tendency for the impingement distribution to be relatively spread out. They also evaluated the stagnation point radial velocity gradient, which was normalized by two ways: based on the conditions at the nozzle exit, and based on the measured local free jet conditions. It was found that for the subsonic jets, the values are nearly similar due to roughly equivalent core lengths and rates of decay. Finally, they presented several wall jet measurements for supersonic jets which are out of the scope of this work.

Bradbury (1972) studied the impact of an axisymmetric jet onto a normal ground. He used two different nozzle configuration with various nozzle exit velocities up to about 120 m/s. Tests were conducted with distance between the nozzle and the ground ranged from 0.054 to 0.254 m.

He used some of the flow features along with the data he obtained to introduce a simple argument for correlating data in the impact region. He used the facts that the flow in the free jet region becomes self similar after six diameters distance, the thickness of the jet becomes proportional, and the mean velocity becomes inversely proportional to the vertical distance after the potential core. This argument was applied to the static pressure on the ground board and to the peak of dynamic head in the flow over the ground board. The nondimensionalized static pressure distribution on the ground board was found to be independent of the height of the nozzle except for low heights in which the flow profiles were not similar before the impingement point. The obtained data showed that the center line static pressure is about 12% above that in the free jets when the ground board is absent. Finally, the data also confirmed the inviscid nature of the flow in the impacting region.

Beltaos and Rajaratnam (1977) performed an experimental and analytical study of developing jets impinging on a smooth wall for small values of nozzle height. The values ranged from 2.21 to 5.17 of nozzle height (h) to nozzle diameter (d) ratio. Despite the results of high h/d values, flow parameters were found to be independent of h whereas they are governed by the diameter and jet velocity. Measurements of the velocity

field, static pressure, and wall shear stresses were reported and analyzed. Semi-empirical methods for predicting the flow field parameters were also developed. It was found that the impinging region extends to $1.2d$ above wall and $1.4d$ radially from the stagnation point. Finally, the growth of the jet from the stagnation point in the radial direction including the wall jet region was plotted and analyzed.

Borges and Viegas (1982) studied the shear stress field produced by the impingement of single and multiple circular jets on normal, oblique, and parallel plane surface. For the single normal impinging jet, the mean shear stress distribution was measured by a Preston tube whereas the shear stress fluctuations were measured with a hot-film sensor. The results of a nondimensionalized shear stress at the wall were compared with those produced from an expression suggested by Beltaos and Rajaratnam (1974) for the impact region and found to be in good agreement. It was shown that the intensity of shear stress fluctuations is small compared with the shear stress mean value.

Araujo *et al.* (1982) used a laser Doppler anemometer incorporating a frequency shift device to measure the mean and fluctuating velocity components in developing jets impacting normally and obliquely on a smooth surface. The nozzle diameter was 14.0 mm and the exit velocity was 50 m/s. It was found that similarity of the nondimensionalized mean axial

velocity is reached at approximately 8 diameters from the nozzle. It is believed that the Reynolds number and the turbulence intensity at the jet exit have influence on the initial spreading of the jet. Further, the center line velocity decay and the jet spreading rate were measured and evaluated by suggested empirical relations. The turbulence intensity was found to be around 20% at a distance of $12d$ downstream the jet exit. In the wall region, the turbulence intensities were high with a minimum value of 35% located around the point of maximum velocity. It also was found that the flow reaches similarity in the radial distance range of 6 to 9 r/d . Empirical relations were presented for the wall jet spreading rate and velocity decay with the radial distance measured from virtual wall jet origin. The virtual wall jet origin was found to be equal to $1.5 d$. It was also demonstrated that the outer shear layer has an important role on the turbulent mixing process.

Curtis (1986, 1987) carried out experimental investigations of the behavior of single wall and free jets. The nozzle, which was of 1 inch diameter, was placed at $h/d = 8.5$. For the wall jet cases, it was found that the characteristics of the flow were unaffected by the pressure ratio of the nozzle which was varied between 1.04 and 3.00. It was stated that the effect of the nozzle height is negligible, hence it was not investigated. This statement is in contrary with previous researchers results (Poreh *et al.*, 1967 and Beltaos and Rajaratnam, 1977) which proved that the flow field of the

wall jet is affected with the nozzle height if it is greater than 8 diameters, i.e., the flow becomes self similar before entering the impingement region. Plots of the ground sheet depth for different nozzle pressure ratios are presented.

Smith *et al.* (1990) studied extensively the jet flow field generated by advanced short take-off and vertical landing (ASTOVL) aircraft in ground effects experimentally and computationally. They studied single-, twin-, and three-jet impingement flow fields. The studies were carried out using several flow visualization techniques such as laser sheet illumination, shadowgraph/schlieren, and dye injection along with ground and under fuselage surface measurements. Regarding the single subsonic jet impingement case, which is of our interest, they presented previous measurements which confirmed that the impingement pressure shows a normal distribution and that the peak pressure depends upon how much the jet is mixed upstream of the impingement.

2.3 Numerical Investigations

In an investigation that is considered to be one of the first attempts to utilize two-equation turbulence models in jet impingement flows, Agarwal and Bower (1982) solved compressible Navier-Stokes and energy equations in conjunction with the well known $k-\epsilon$ turbulence model for a planar impinging jet configuration relevant to VTOL aircraft design. The equations were solved in stream function/vorticity form and the physical domain was mapped conformally into a rectangular computational region. They used an augmented central-difference scheme in order to preserve the diagonal dominance character of the difference equations at high Reynolds numbers. The resulting difference equations were solved by a point successive over relaxation (SOR) algorithm. Three different cases were studied; incompressible turbulent impinging jet with and without upper surface and compressible turbulent impinging jet with an upper surface. Plots for ground plane pressure, fuselage under surface pressure, the centerline velocity, and turbulent kinetic energy distributions along with stream function and vorticity contours were presented. The computed results of the pressure and velocity were found to be in good agreement with previous experimental data. However, the computed turbulent energy along the jet axis showed a large overshoot near the ground plane. This was attributed to

deficiency in the turbulence model. It was concluded that, unlike the zero and one-equation models, the two-equation model can predict accurately the velocity and pressure fields, which are the quantities of primary interest in VTOL aircraft design.

Glynn and Jal (1987) used the commercially available finite volume code "PHOENICS" to solve axisymmetric free and impinging jets' flow fields. Regarding the impinging jet, they studied three different jet exit velocities with fixed nozzle height to nozzle diameter ratio of 8.5 and a radial distance of 12 nozzle diameter. The jet exit turbulence intensity was assumed to be 1% while the length scale was 3.5% of the nozzle diameter. A fully elliptic calculation procedure was adopted with three different grids. A medium type grid of 65 radial by 55 vertical cells was found to give optimum results in terms of accuracy and computational time. The standard $k-\epsilon$ model was initially used to predict the flow field properties. Comparing the results with the experimental data of Poreh *et al.* (1967) and Curtis (1986, 1987) showed an underprediction in wall jet spreading. This may be attributed, at least in part, to the truncation error raised from inadequate extent of the flow field. Furthermore, the results showed that the effect of varying the pressure ratio of the nozzle, i.e. the exit velocity, is very small and hence agreeing with Curtis' findings. Finally, two modifications to the standard coefficients were implemented. The Rodi (1980) free jet correction

was used in the free jet region and below it the wall jet modification of Malin (1987) was incorporated whereas no correction had been used in a small region near to the point of impingement. These modifications yielded to some improvements in the prediction of the spreading of the wall jet.

Hwang and Liu (1989) performed a numerical study of the two dimensional impinging jet flow field relevant to VTOL aircraft. They employed the Reynolds-averaged compressible Navier-Stokes, continuity, and energy equations for two cases: turbulent impinging jet with free upper surface and laminar impinging jet with upper flat surface. For the turbulent jet case, the flow field equation were solved in conjunction with a two-equation $k-\epsilon$ model. Beam and Warming numerical scheme was used with three-point-backward temporal differencing, local linearization, and factorization. The difference equations were solved by the alternating direction implicit (ADI) sequence. The ground plane pressure distribution was plotted and found to be in good agreement with experimental data. Furthermore, plots of the maximum velocity growth and the skin friction along the wall compared with previous experimental data were presented.

Bray (1991) performed extensive experimental and computational investigations for free, impinging, and impinging jets in cross flow. He used the "PHOENICS" code with the standard $k-\epsilon$ model and wall function to predict the flow field. For the impingement of a single jet without cross

flow, six cases were studied with different pressure ratios, nozzle height to nozzle diameter ratios, and turbulence intensities. The obtained results were compared with those conducted experimentally by Poreh *et al.* (1967) and Curtis (1986) along with the computational results of Glynn and Jal (1987). In general, reasonable agreement with experimental data was obtained in terms of jet spreading rate, velocity decay rate and velocity profiles. However, the wall jet thickness appeared to be slightly overpredicted close to the impinging region and underpredicted beyond the impinging region where the rate of thickness growth is significantly underpredicted. It was believed that the initial overprediction in wall jet thickness is caused by the overprediction in free jet spreading whereas the underprediction downstream is due to shortcomings in the $k-\epsilon$ model and the use of the law-of-the-wall functions to bridge the viscous sublayer. The results also showed that the effects of the nozzle height, nozzle exit velocity, and nozzle exit turbulence intensity are negligible. Furthermore, the obtained velocity profiles were in error in the near wall region. This also was attributed to the logarithmic law-of-the-wall functions. Finally, Bray presented plots for nondimensionalized wall jet maximum velocity decay along the radial distance. The results showed an underprediction of the maximum velocities especially in the vicinity of the impinging region.

McGuirk (1991) presented a synopsis of the computational results from a Lyon/IAHR workshop. From the thirteen participated investigations, seven had used the standard $k-\epsilon$ model, five had used Reynolds stress model, and one had used the two-layer model whereas no one had used any modified $k-\epsilon$ model nor the algebraic stress model. It was concluded that still there were model/model and model/data differences. Also, the results were very sensitive to some boundary conditions practices especially for the wall and the entrainment boundaries.

Craft and Launder (1991, 1992) used three different turbulence models to predict the flow field and the stresses in an impinging jet case. A modified $k-\epsilon$ model, a Reynolds stress model, and a new wall-reflection Reynolds stress model were tested and compared with previous experimental data. The modified $k-\epsilon$ model which introduces a Yap correction was found to be effective in reducing near-wall length scales in the stagnation region. Although the Reynolds stress model gave slightly better results than the $k-\epsilon$ ones, the new model, which reduces the stress normal to the wall, resulted in considerably better prediction.

Chapter 3

Mathematical Modeling

3.1 Introduction

In many engineering design problems, computer modeling is considered as a complementary and supplementary tool to aid design procedures (Sloan *et al.*, 1982). This is because it, in general, gives adequate accurate predictions which can be used for further and more accurate techniques. Thus, computational fluid dynamics (CFD) had become an effective tool in solving several complicated fluid and heat transfer problems.

A preliminary copy of the computer code TEAM is used in all the CFD predictions carried out in this work. TEAM, an acronym for Turbulent Elliptic Algorithm - Manchester, is a finite-difference / finite-volume computer code for the simulation of two dimensional turbulent elliptic flows (Huang and Leschziner, 1983). It was developed from the previous code TEACH with several improvements in order to achieve a better

performance. The code can be applied to plane and axisymmetric flows with different boundary conditions.

In this copy of the TEAM code, turbulence is represented by the widely used $k-\varepsilon$ model. The present author had introduced two other turbulence models namely: the two-layer model, and the algebraic stress model.

3.2 Governing Equations

Performing Reynolds decomposition and time averaging, the instantaneous equations of change are transformed to mean equations of change which contain new unknowns known as Reynolds stresses. For steady, incompressible, two-dimensional, and axisymmetric flows, these mean quantities equations can be written as follows (Sloan *et al.*, 1986):

Continuity

$$\frac{\partial U}{\partial x} + \frac{1}{r} \frac{\partial V}{\partial r} (rV) = 0 \quad (3.1)$$

Axial momentum

$$\rho \frac{\partial}{\partial x} (UU + \overline{uu}) + \frac{\rho}{r} \frac{\partial}{\partial r} (rVU + r\overline{uv}) = \frac{\partial}{\partial x} \left(\mu \frac{\partial U}{\partial x} \right) + \frac{1}{r} \frac{\partial}{\partial r} \left(r\mu \frac{\partial U}{\partial r} \right) - \frac{\partial p}{\partial x} + \frac{\partial}{\partial x} \left(\mu \frac{\partial U}{\partial x} \right) + \frac{1}{r} \frac{\partial}{\partial r} \left(r\mu \frac{\partial V}{\partial r} \right) \quad (3.2)$$

Radial momentum

$$\rho \frac{\partial}{\partial x} (UV + \overline{uv}) + \frac{\rho}{r} \frac{\partial}{\partial r} (rVV + r\overline{vw}) = \frac{\partial}{\partial x} (\mu \frac{\partial V}{\partial x}) + \frac{1}{r} \frac{\partial}{\partial r} (r\mu \frac{\partial V}{\partial r}) - \frac{\partial \phi}{\partial r} + \frac{\partial}{\partial x} (\mu \frac{\partial U}{\partial x}) + \frac{1}{r} \frac{\partial}{\partial r} (r\mu \frac{\partial U}{\partial r}) - 2\mu \frac{V}{r^2} \quad (3.3)$$

where \overline{uu} , \overline{uv} , and \overline{vw} are the new unknowns which are treated by different approaches depending on the turbulence model.

k-ε model

The Reynolds stresses in the k-ε model are prescribed using the Boussinesq' or the eddy-viscosity concept which assumes that the Reynolds stresses are proportional to the mean-velocity gradients (Rodi, 1980). This concept can be expressed as

$$-\rho \overline{u_i u_j} = \mu_t \left(\frac{\partial U_i}{\partial x_j} + \frac{\partial U_j}{\partial x_i} \right) - \frac{2}{3} k \delta_{ij} \quad (3.4)$$

where the eddy (or turbulent) viscosity μ_t is calculated from

$$\mu_t = C_\mu \frac{k^2}{\epsilon} \quad (3.5)$$

and δ_{ij} is the Kronecker delta.

Here, full transport equations for the turbulence kinetic energy (k) and its energy dissipation (ε) are used. The implementation of the above assumptions results in the following form of equation for φ which relates to density, momentum, and turbulence quantities k and ε.

$$\frac{\partial}{\partial x}(\rho U \phi) + \frac{\partial}{\partial r}(\rho V \phi) = \frac{\partial}{\partial x}(r \Gamma^\phi \frac{\partial \phi}{\partial x}) + \frac{\partial}{\partial r}(r \Gamma^\phi \frac{\partial \phi}{\partial r}) + r S^\phi \quad (3.6)$$

The expressions of the turbulent exchange coefficient Γ^ϕ and the source term S^ϕ are listed in Table 3.1.

Table 3.1: Exchange coefficients and sources.

Equation	ϕ	Γ^ϕ	S^ϕ
Continuity	1	0	0
Axial momentum	U	μ_{eff}	$-\frac{\partial p}{\partial x} + \frac{\partial}{\partial x}(\mu_{\text{eff}} \frac{\partial U}{\partial x}) + \frac{1}{r} \frac{\partial}{\partial r}(r \mu_{\text{eff}} \frac{\partial V}{\partial r})$
Radial momentum	V	μ_{eff}	$-\frac{\partial p}{\partial r} + \frac{\partial}{\partial x}(\mu_{\text{eff}} \frac{\partial U}{\partial r}) + \frac{1}{r} \frac{\partial}{\partial r}(r \mu_{\text{eff}} \frac{\partial V}{\partial r}) - \frac{2\mu_{\text{eff}} V}{r^2}$
Turbulence energy	k	$\mu_{\text{eff}}/\sigma_k$	$G - \rho \epsilon$
Energy Dissipation	ϵ	$\mu_{\text{eff}}/\sigma_\epsilon$	$\frac{\epsilon}{k}(C_1 G - C_2 \rho \epsilon)$

In Table 3.1 above G is the production (or generation) of the turbulent energy and μ_{eff} is the effective viscosity and they are defined as follows:

$$G = \mu_t \left\{ 2 \left[\left(\frac{\partial U}{\partial x} \right)^2 + \left(\frac{\partial V}{\partial r} \right)^2 + \left(\frac{V}{r} \right)^2 \right] + \left(\frac{\partial U}{\partial r} + \frac{\partial V}{\partial x} \right) \right\} \quad (3.7)$$

$$\mu_{\text{eff}} = \mu + \mu_t \quad (3.8)$$

Table 3.2 lists the standard k- ϵ turbulence model's constants.

Table 3.2: Standard k-ε turbulence model's constants.

C_μ	C_1	C_2	σ_k	σ_ϵ
0.09	1.44	1.92	1.0	1.22

The two-layer model

In this investigation, a two-layer model which combines the k-ε model and a simple one-equation model is tested. The standard k-ε model is used to solve for the flow field not too close to the wall whereas a one-equation model is used to resolve the viscosity affected region near the wall. The one-equation model of Norris and Reynolds (Rodi, 1991) was tested in which the eddy viscosity μ_t is calculated by

$$\mu_t = \rho f_\mu C_\mu' \sqrt{k} L \quad (3.9)$$

where

$$C_\mu' = 0.084$$

$$f_\mu = 1 - \exp(-R_y/A), \quad (3.10)$$

$$R_y = \frac{\sqrt{k} y_n \rho}{\mu}, \quad (3.11)$$

$$L = C_D \kappa y_n, \quad (3.12)$$

$$C_D = 6.41,$$

$$A = 50.5$$

$$\kappa = .41,$$

and y_n is the normal distance from the wall.

For the turbulent quantities, no transport equation for the dissipation ε is there and hence ε in the source term of the turbulent energy is replaced with the following expression:

$$\varepsilon = \frac{k^{3/2}}{L} \left(1 + \frac{\mu C_\varepsilon}{\sqrt{k} L \rho} \right) \quad (3.13)$$

where $C_\varepsilon = 13.2$.

The two-equation model and the one-equation model are matched by different methods. Some researchers matched the two models at a preselected grid line where others matched them at a location where a certain criterion is satisfied (Rodi, 1991). Two criteria were tested: one is to match the two models at a location where the ratio of eddy viscosity to the molecular viscosity has a certain high value. The second criterion is to match the models where the damping function (f_μ) has a value close to unity. Both of the criteria insures that the viscous effects are small and hence the two-equation k- ε model is implemented just in the free turbulent region.

The algebraic stress model

Full Reynolds stress models employ transport equations for the Reynolds stresses of the form (Launder *et al.*, 1975)

a portion of the Reynolds stresses to be inserted into the diffusion terms of the momentum equations instead of the entire quantity being incorporated into the source term. This was found to produce more diagonally dominant coefficient matrix and hence to converge more quickly.

The entire algebraic stress equation set along with the production terms are presented in Appendix A whilst different suggestions for the constants C_{s1} , and γ are listed in Table 3.3.

Table 3.3: Algebraic stress model constants.

C_{1s}	γ	Reference
1.5	.6	(Launder <i>et al.</i> , 1975) & (Liou <i>et al.</i> , 1992)
1.8	.6	(Andersson and Nilsen, 1989)
2.2	.55	(Launder, 1975) & (Childs and Patel, 1990)

3.3 Grid Layout

The practice used in the computer code TEAM for layout the grid involves defining the control volumes and placing the associated grid points in the volume centers. It is believed that this practice gives better resolution in turbulent flow calculations. A staggered grid system is used where the scalar quantities such as pressure, turbulent energy, energy dissipation, and

$$I_e - I_w + I_n - I_s = \int_{\Delta Vol} S_\phi dVol \quad (3.16)$$

where I_f represents the total flux of the scalar variable ϕ across the control volume face f ($f = e, w, n, \text{ or } s$; see Figure 3.1). The surface flux I_f contains a convective contribution I_f^C and a diffusion contribution I_f^D :

$$I_f = I_f^C + I_f^D \quad (3.17)$$

$$= \text{mass flux at face } f * \text{Geometric quantity} * \phi_f$$

$$- \text{diffusivity at face } f * \text{Geometric quantity} * (\phi_p - \phi_f)$$

The most difficult task in evaluating these surface integrals is to approximate a value for the scalar variable ϕ at the surface of the control volume. The determination of ϕ_f is a key element for the accuracy and the stability of numerical solution. Two different schemes are built in TEAM to approximate ϕ_f : the Power Law Differencing Scheme (PLDS) and the Quadratic Upstream-Weighted Differencing Scheme (QUICK). PLDS was found to be more stable but, false diffusion is associated with it. QUICK seemed to be more accurate but tends to produce overshoots.

The source term S_ϕ is assumed to be uniform over the control volume. It is linearized as

$$S_\phi = S_\phi^U + S_\phi^P \phi_p \quad (3.18)$$

In order to enhance the stability of the numerical process, S_ϕ^P is defined so that it is always not larger than zero for all the conservation equations, and S_ϕ^U always assumes non-negative values for both k- and ϵ -equations (Zhu, 1991).

The final form of the discretized equations reads:

$$a_\phi^P \phi_p = a_\phi^E \phi_E + a_\phi^W \phi_W + a_\phi^N \phi_N + a_\phi^S \phi_S + S_\phi^U \Delta x \Delta y \quad (3.19)$$

The resulting finite difference equations are solved by a line-iterative method using a Tri-Diagonal Matrix Algorithm (TDMA) with alternating sweep directions. This algorithm is closely akin to the ADI techniques. To solve the system of nonlinear algebraic equations deduced from the

algebraic stress model, the Newton method for nonlinear systems (Burden *et al.*, 1978) is used in subiterations.

3.5 Treatment of velocity-pressure coupling

When solving incompressible fluid flow problems in terms of primitive variables, a difficulty arises due to the absence of an equation explicitly governing the pressure. To solve this problem, indirect methods are used to obtain the pressure field. Two different algorithms for handling the velocity-pressure coupling are implemented in TEAM: the “Semi Implicit Method for Pressure Linked Equations” method (SIMPLE) (Patankar, 1980) and the “Pressure Implicit Solution by Split Operator” method (PISO). The sequence of operations for SIMPLE and PISO is illustrated in Figure 3.2.

3.6 Boundary conditions

The above set of differential equations are elliptic in nature, and therefore require specifying boundary conditions on all the domain boundaries. Boundaries can be of five different types: fluid entry plane, fluid exit plane, axis of symmetry, entrainment boundary, and wall. In the present case, all these boundaries exist and they are shown in Figure 3.3 and discussed below.

3.6.1 Fluid entry plane

This boundary is presented by the exit of the nozzle in the present work. All the fluid and the flow properties are prescribed along this boundary. Uniform normal velocity and pressure profiles are assumed whereas the tangential velocity component is set to zero. For the turbulent quantities, the turbulent energy and the energy dissipation are formulated by the following expressions:

$$k_{in} = (TI U_{in})^2 \quad (3.20)$$

$$\varepsilon_{in} = \frac{0.015 k_{in}^{3/2}}{0.035 d_n} \quad (3.21)$$

where TI is the turbulence intensity and d_n is the nozzle diameter. The turbulence intensity is taken as 0.03. These formulations were used by Bray (1991) and Baha (1994).

3.6.2 Fluid exit plane

Along this boundary, uniform pressure is prescribed and zero streamwise gradients of all the properties are implemented. The tangential component of the velocity is calculated directly from the continuity equation.

3.6.3 Axis of symmetry

The gradients of all the properties normal to the axis of symmetry and the normal velocity component are zero. This is easily implemented by setting the coefficient $a_s = 0.0$.

3.6.4 Entrainment boundary

This boundary is treated as the fluid exit boundary, i.e. constant pressure profile and zero streamwise gradients of all the properties.

3.6.5 Wall boundary

For both the k- ϵ model and the algebraic stress model, the wall function approach (Launder and Spalding, 1974) is used in which the resultant wall shear stress is related to the flow velocity vector by

$$\tau_w = -\lambda_w \vec{V}_p \quad (3.22)$$

where

$$\lambda_w = \begin{cases} \mu / y_p & \text{if } y_p^* < 11.63 \\ \rho C_\mu^{1/4} k_p^{1/2} \kappa / \ln(E y_p^*) & \text{otherwise} \end{cases} \quad (3.23)$$

$$y_p^* = \rho C_\mu^{1/4} k_p^{1/2} y_p / \mu \quad , \quad (3.24)$$

$$E = 9.7.$$

The subscript P refers to the first control volume center from the wall. Moreover, the diffusive flux of the turbulent energy is set to zero and the near wall values of the generation and energy dissipation are determined by

$$G_P = \frac{\tau_w^2}{\kappa \mu y_p^+} \quad (3.25)$$

$$\varepsilon_p = \frac{C_\mu^{3/4} k_p^{3/2}}{\kappa y_p} \quad (3.26)$$

For the two-layer model, the velocities and the turbulent energy are set to zero at the wall.

The algebraic expressions given for ε degenerate at the wall, but the value of ε is not needed exactly at the wall. This is also correct for the values of the Reynolds stresses in the algebraic stress model.

3.7 Sequence of Solution Steps

The main solution steps can be summarized as follows:

1. Initialize the variable field U, V, P, k, and ε .
2. For the algebraic stress model, initialize the Reynolds stresses field.
3. Calculate the effective transport coefficients.
4. Assemble the coefficients for U- momentum equation.
5. Impose the boundary conditions by modifying the coefficients and sources.
6. Solve for the U- field.
7. Similar to steps 4-6, solve for V- field.
8. Similar to steps 4-6, solve for P_1 .

9. Adjust velocities.
10. If PISO is used, solve for P_2' .
11. Update pressure.
12. Similar to steps 4-6, solve for k - field.
13. Similar to steps 4-6, solve for ϵ - field.
14. For algebraic stress model, solve for the Reynolds stresses.
15. Repeat steps 3 through 14 until the specified convergence criterion is reached.

3.8 Solution Procedure

3.8.1 Convergence criterion

The iterative procedure is considered to yield a converged solution if the absolute normalized residuals for U , V , K , and ϵ along with the mass source are less than a prescribed small value. The velocities U and V are normalized by the total inflow momentum, while k , and ϵ are normalized by the product of the total volumetric inflow and inlet values of k , ϵ respectively. The mass source is normalized by the total inflow of mass. The prescribed value, i.e. the convergence criterion, is dependent on the needed degree of accuracy of the solution.

3.8.2 Under-relaxation

Under-relaxation is a means of slowing down the rate of convergence of the solution process. Although this seems to be undesirable, it is found to be necessary to ensure convergence since it avoids steep rates of change in the variables. It also provides a means of equalizing the rates of the various non-linear coupled equations. In this work, a linear under-relaxation introduced in an implicit fashion is used. It is done as follows

$$\phi^{I+1} = \phi^I + URF (\phi^{I+1} - \phi^I) \quad (3.27)$$

where ϕ^I is the value of the general variable ϕ at iteration number I , ϕ^{I+1} is the value of ϕ at iteration number $I+1$ and URF is the under-relaxation factor which is chosen depending on experience and trial and error.

3.8.3 Multi-grid technique

The present author had modified TEAM to use the multi-grid technique in order to improve convergence and reduce number of iterations and, hence, computational efforts. The basic idea of this scheme is to run the program for coarse grid case and then, with a suitable interpolation procedure, feed the interpolated results as the initial values for a fine grid. This was found to be superior in reducing the computational time. This technique was recommended by different researchers (see Ferziger, 1987).

3.8.4 Solution strategy

Extensive work and very preliminary runs were made with the $k-\epsilon$ model in order to ensure grid independence and to get suitable grid points distribution. The next step was to enable the two-layer model and the algebraic stress model. The same strategy was recommended and used by Childs and Patel (1990).

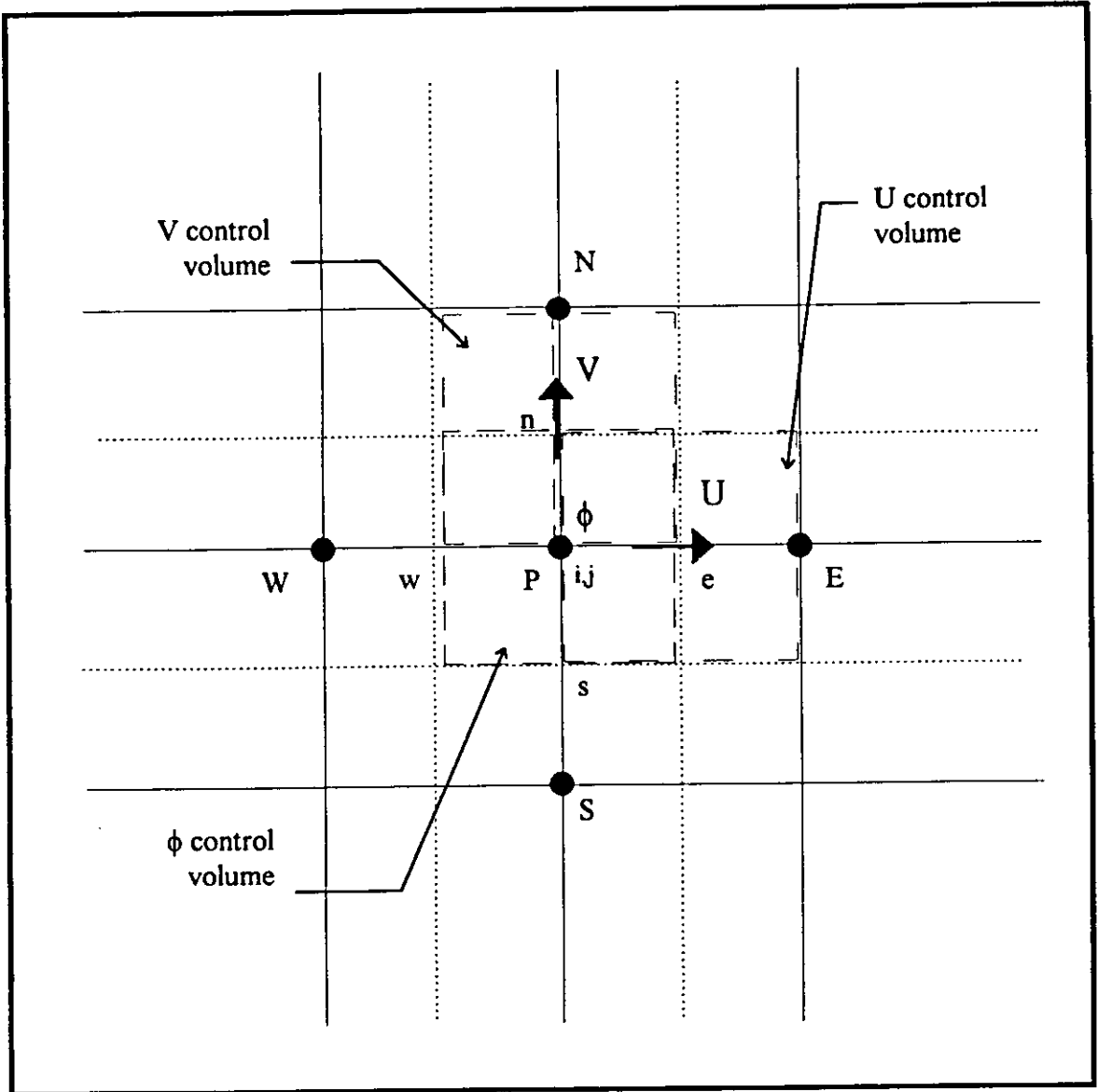


Figure 3.1: Grid layout and control volumes and surfaces.

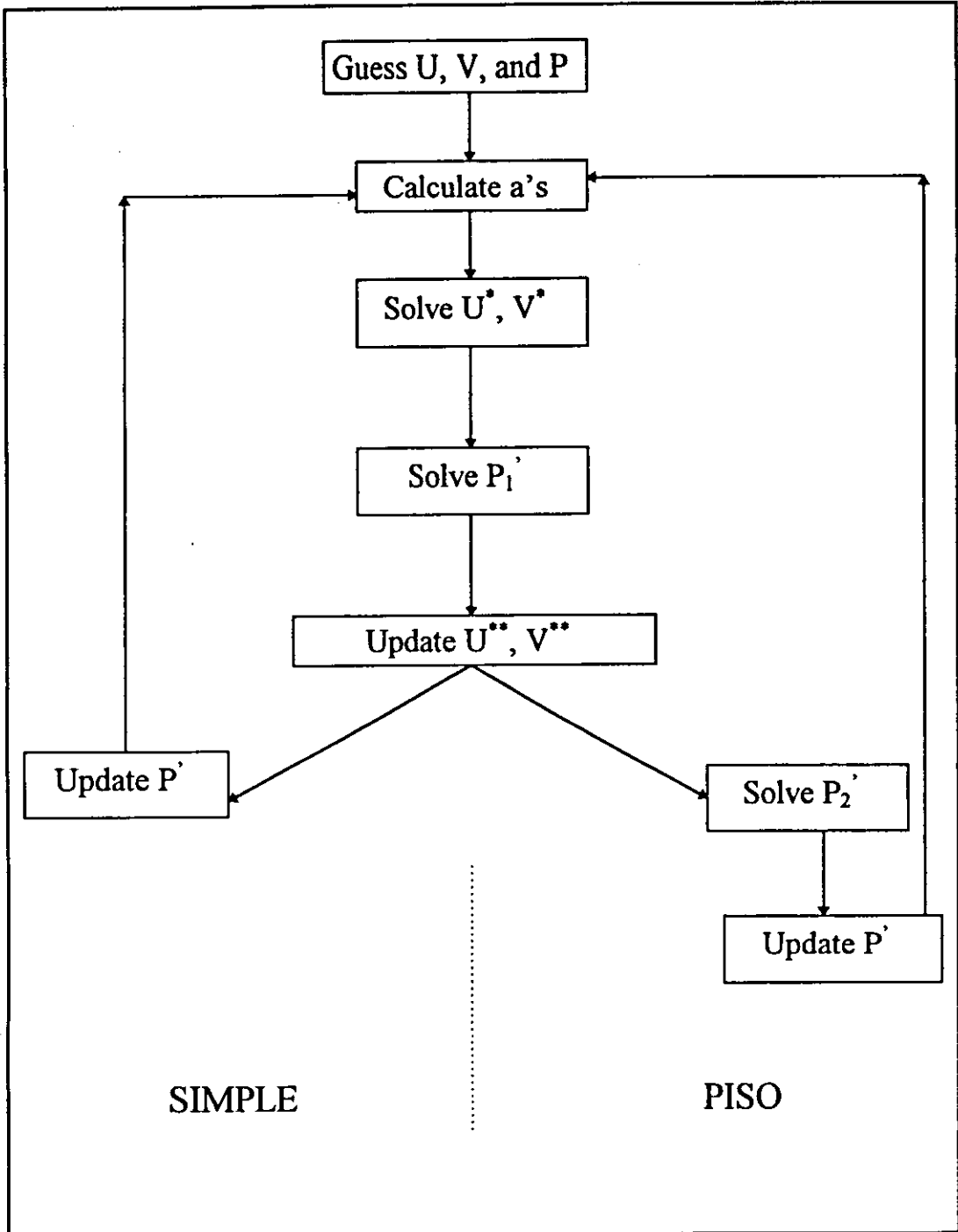


Figure 3.2: Flow diagrams for SIMPLE and PISO.

Chapter 4

Results and Discussions

4.1 Introduction

In this investigation, two cases were studied to explore the suitability of the tested turbulence models in predicting the flow field of an impinging jet problem. These two cases were chosen in a manner that facilitates comparisons with previous experimental and computational results. Case 1 is comparable with the experimental work of Poreh *et al.* (1967) whereas case 2 is comparable with the experimental work of Curtis (1986). Bray (1991) had conducted computational investigations using the $k-\epsilon$ model for the two cases. Both of the cases were solved by the $k-\epsilon$, the algebraic stress, and the two-layer models. A listing of the two cases parameters is given in Table 4.1.

Table 4.1: The parameters of the tested cases.

Parameter	Case # 1	Case # 2
Nozzle diameter, d (m)	0.0254	0.0254
Nozzle height, h (m)	0.6096	0.2159
Nozzle pressure ratio, P_m	1.079	1.05
Nozzle exit velocity U_{in} (m/s)	112.8	90.0
Turbulence intensity	0.03	0.03
Total radial distance (m)	0.7	0.6177
Grid points	70*70	70*70

Preliminary runs were conducted and much time was spent in order to investigate the reliability of the computer code TEAM and the proper grid specifications. In order to confirm our results, case 1 was solved by the $k-\epsilon$ model with the same grid specifications used by Bray (1991). The results showed very good agreement with those of Bray and they are plotted in Figure 4.1. After several runs with different number of grid points, it can be stated that grid independence is achieved for case 2, Figure 4.2. Although the height of the nozzle in case 1 is greater than that for case 2, the same number of grid points was used axially in order to test the effect of the grid spacing on the performance of the turbulence models. To improve convergence, multi-grid technique was used along with under relaxation

factors ranged from 0.5 to 0.7. Furthermore, smoothly spaced grid was used, that is $.9 < \Delta x_i / \Delta x_{i+1} < 1.15$, which concentrates grid lines near the jet exit and the wall. The present investigation initially was carried out on VAX 8700 available at University of Jordan. A typical iteration consumed about 4 seconds. After that, the predictions were performed on a Pentium 133 PC with which the elapsed time became less than a second for the iteration. The algebraic stress model predictions consumed about one and half of the stated time above since subiterations are made to converge the Reynolds stresses at each iteration. In general, a residual 0.01% was typical for the continuity and momentum equations while 1% was accepted for the turbulence quantities since in most cases, the turbulence energy dissipation could not be converged to less than 1%. This also was faced in Bray (1991) and Baha (1994) works. Moreover, 1000 iterations were sufficient to converge the k- ϵ model with the multi-grid technique introduced to the code by the present worker. The same number of iterations gave a converged solution for the algebraic stress model with the decomposition of the Reynolds stresses which was illustrated in the previous chapter. With the results of the k- ϵ model being as initial guess, around 1750 iterations were needed to converge the two layer model.

4.2.2 Maximum velocity decay

Figures 4.6 and 4.7 show the maximum velocity decay curves deduced from the k - ε model results for the both cases. The two figures use Poreh's method for non-dimensionalizing the wall jet maximum velocity and radial distance with h/\sqrt{KM} and h respectively. Here the kinematic momentum flux (KM) is defined by (Poreh, 1967)

$$KM = .153 \pi d^2 U_{in}^2 \quad (4.1)$$

For case 1, the maximum velocity values obtained are in good agreement with the experimental results of Poreh near the impingement region whereas they are overpredicted downstream. For case 2, where the grid spacing is smaller, a very good agreement with the experimental data is achieved.

4.3 Algebraic stress model results

4.3.1 Jet spreading rate

Figure 4.8 shows the spreading of the wall jet thickness normalized with the nozzle height against the normalized radial distance for case 1. The obtained results show good improvement for both the wall jet thickness values and the spreading rate over that of Bray. This improvement is clearly observed in case 2, Figure 4.9, where very good agreement with the experiment

results is achieved. This also can be found in Figure 4.10 where the algebraic stress model results for case 2 are compared with that of Curtis.

4.3.2 Maximum velocity decay

The curve of the normalized maximum of case 1 is drawn in Figure 4.11 along with the experimental data of Poreh and the computations of Bray. Again, the maximum velocity is well predicted initially and is overpredicted away from the impingement region. For case 2, where the grid spacing is smaller, this error of results downstream is overcome and good agreement with Poreh's data is obtained, Figure 4.12.

4.4 Two-layer model results

4.4.1 Jet spreading rate

The wall jet thickness results for case 1 are presented in Figure 4.13. The results show a clear overprediction of the jet thickness and an underprediction of the rate of spreading in the region of r/h between 0.4 and 0.6 whereas the prediction is improved slightly downstream. This is attributed to the grid spacing since this trend is not seen in case 2 (see Figure 4.14) where the obtained results exhibit some improvement when compared with Bray results especially near the impingement region. This improvement can also be seen in Figure 4.15 where the results are compared with Curtis findings.

4.4.2 Maximum velocity decay

Figure 4.16 presents the results of the normalized maximum velocity values along the radial distance for case 1. As Bray computational results, the maximum velocity values are underpredicted initially. However, overprediction is noticed down stream. This deviation in the prediction is not seen in case 2 where the results are in very good agreement with the experimental data (see Figure 4.17). This is again attributed to the smaller grid spacing used in case 2.

4.5 Turbulence models comparisons

Regarding the wall jet thickness, results of the three tested models are compared for case 1 in Figure 4.18. It is clear that the algebraic stress model and the $k-\epsilon$ model tend to give almost the same predicted results although little improvement over the $k-\epsilon$ model results is achieved by the algebraic stress model. The two-layer model tends to be much less satisfactory for predicting the wall jet thickness than the other two models. For case 2, the two-layer model predicts the wall jet thickness good near the impinging region whilst it underpredicts the rate of spreading and hence yields to a noticeable underprediction of the wall jet thickness downstream. The

algebraic stress model and the $k-\epsilon$ model are seen to be superior in predicting both the wall jet thickness and its spreading rate (see Figures 4.19, 4.20). The slopes of the wall jet thickness curves, i.e. the rate of spreading of the jet, are presented in Table 4.2 for the different models tested along with those of Poreh and Bray.

Table 4.2 : Comparisons of the slopes of the wall jet thickness curves.

Results	Case 1	Case 2
Poreh (Experiment)	0.085	0.085
Bray ($k-\epsilon$ model)	0.059	0.062
Present ($k-\epsilon$ model)	0.0655	0.073
Present (Algebraic stress model)	0.0675	0.073
Present (Two-layer model)	0.061	0.061

Figure 4.21 compares the maximum velocity decay results of the three tested models for case 1. Here, the algebraic stress model shows a very little improvement over the $k-\epsilon$ model, where the two-layer model gives unsuitable results. However, the two-layer model shows good performance in case 2 and gives slightly better results than the $k-\epsilon$ and the algebraic stress models. This is seen clearly in Figure 4.22 and this ensures the effect of fine grid spacing used.

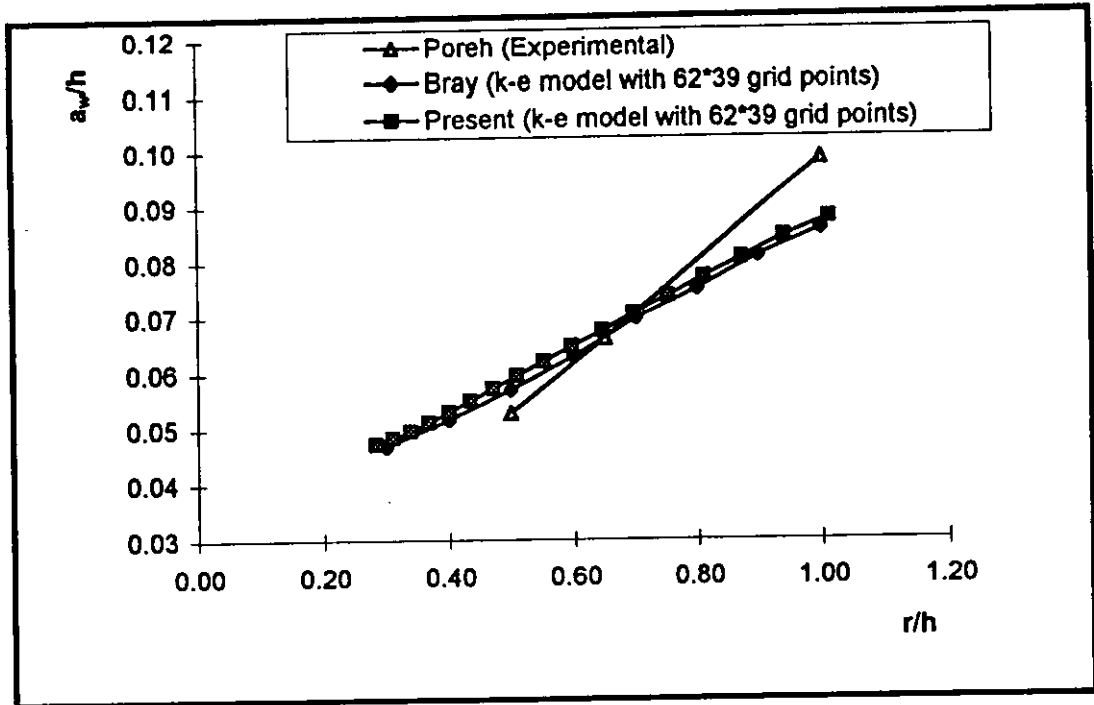


Figure 4.1: Comparison between Bray's results and present results using $k-\epsilon$ model and same grid specification.

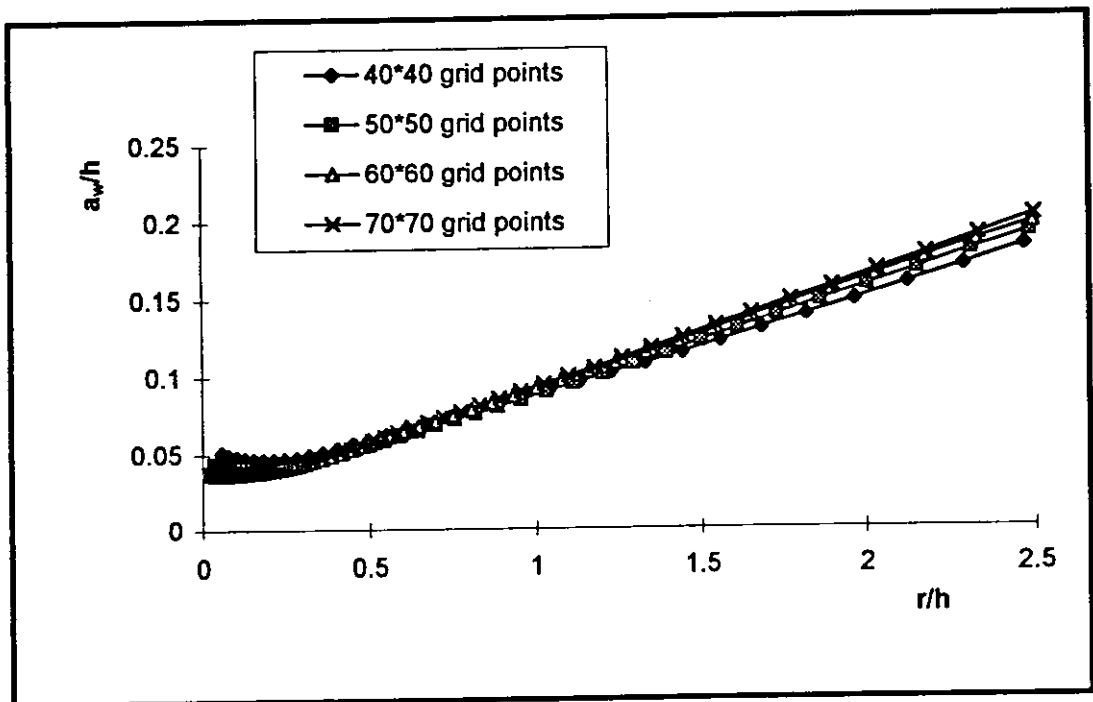


Figure 4.2: Grid independency test for case 2.

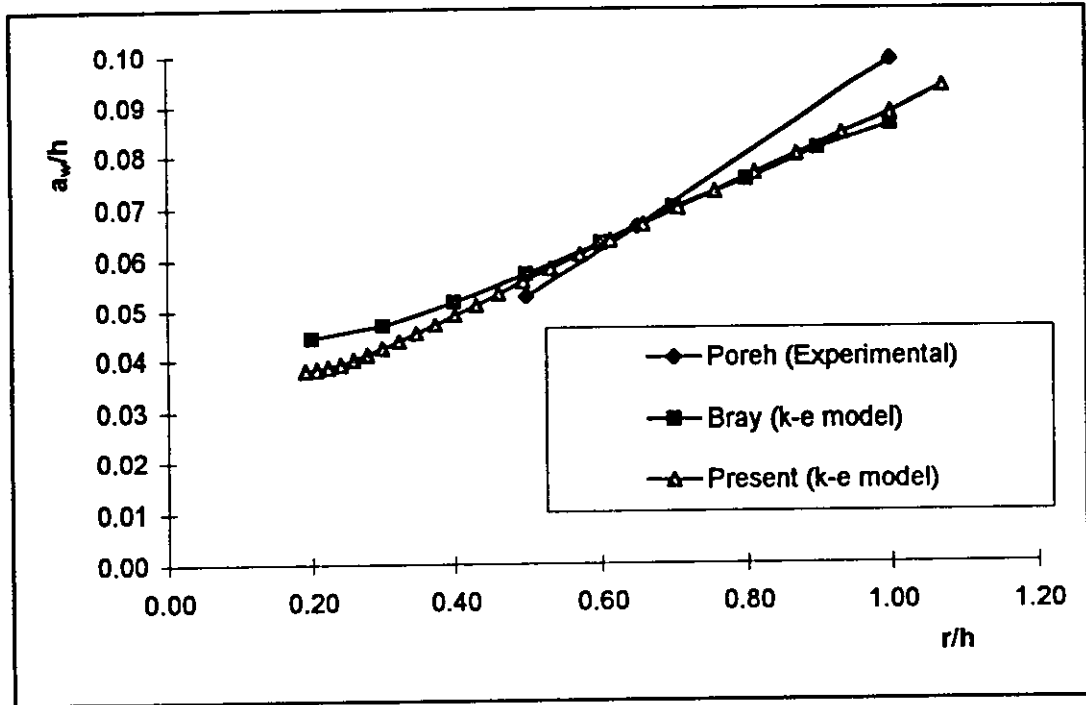


Figure 4.3: Wall jet spreading with r/h for $k-\epsilon$ model: case 1.

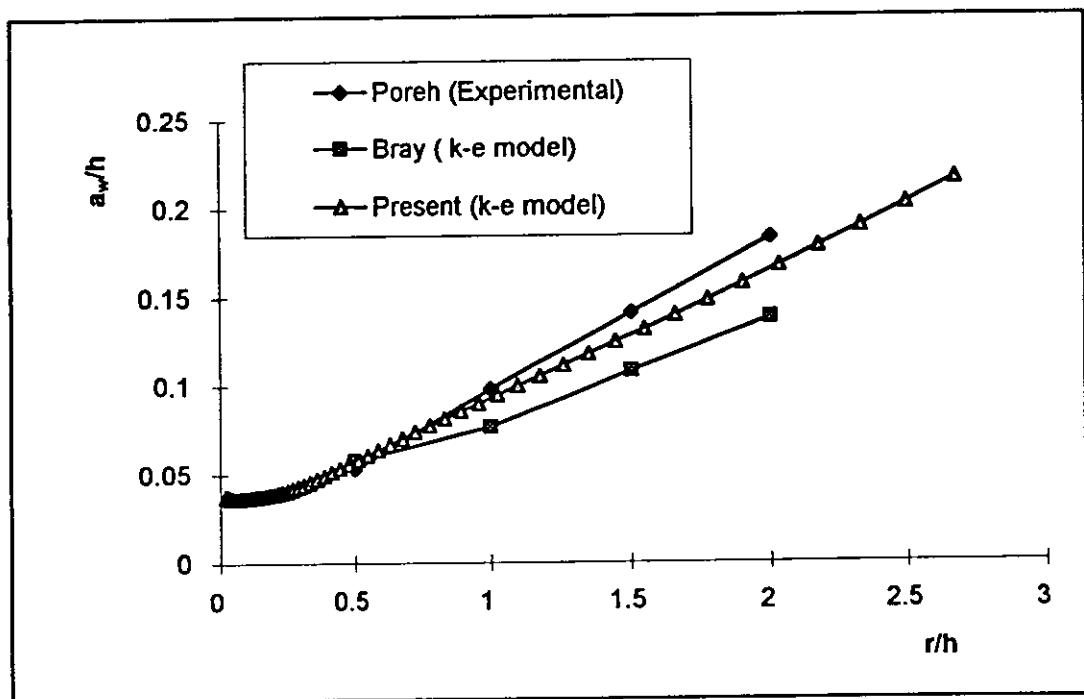


Figure 4.4: Wall jet spreading with r/h for $k-\epsilon$ model: case 2.

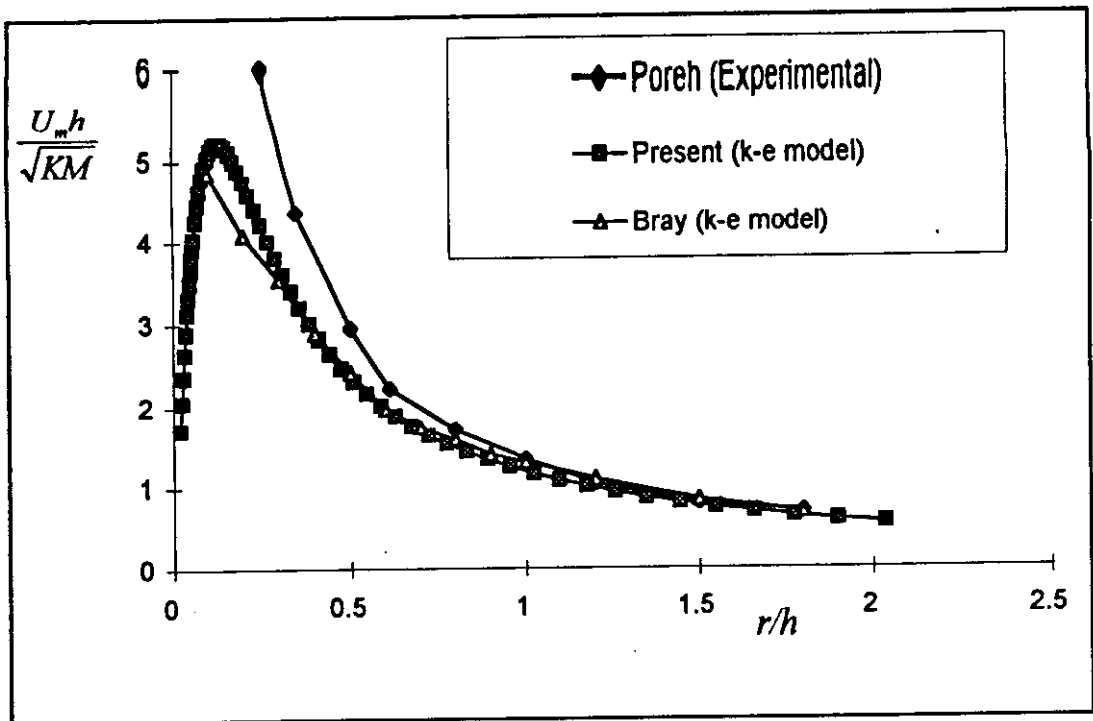


Figure 4.7: Wall jet velocity decay against r/h for $k-\epsilon$ model: case 2.

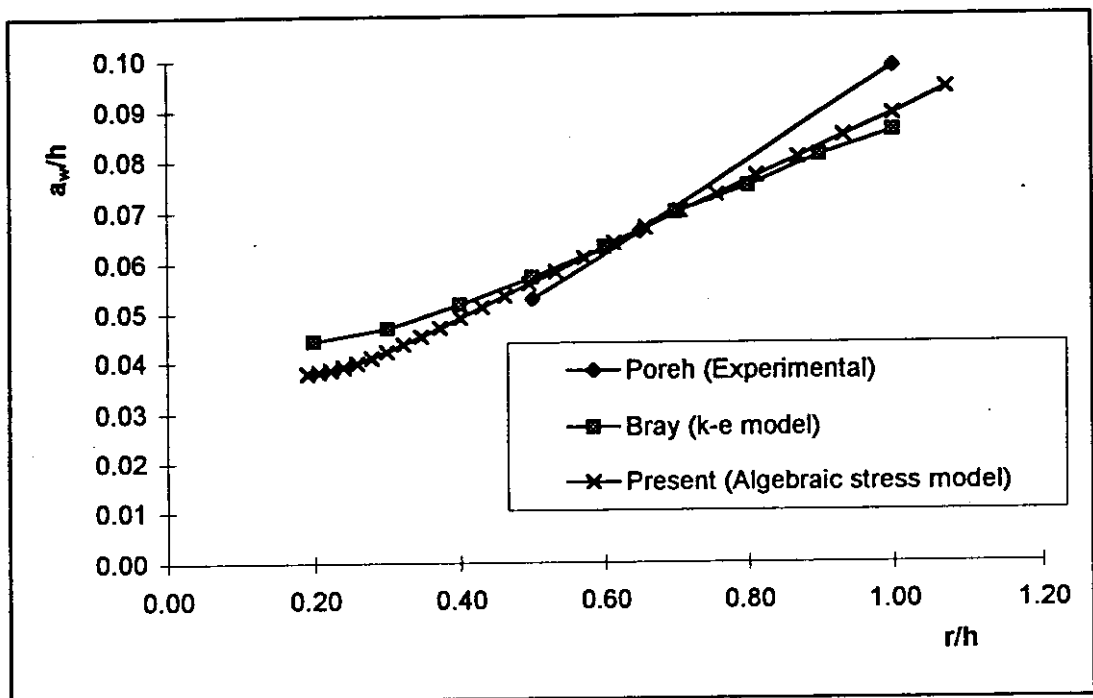


Figure 4.8: Wall jet spreading against r/h for ASM: case 1.

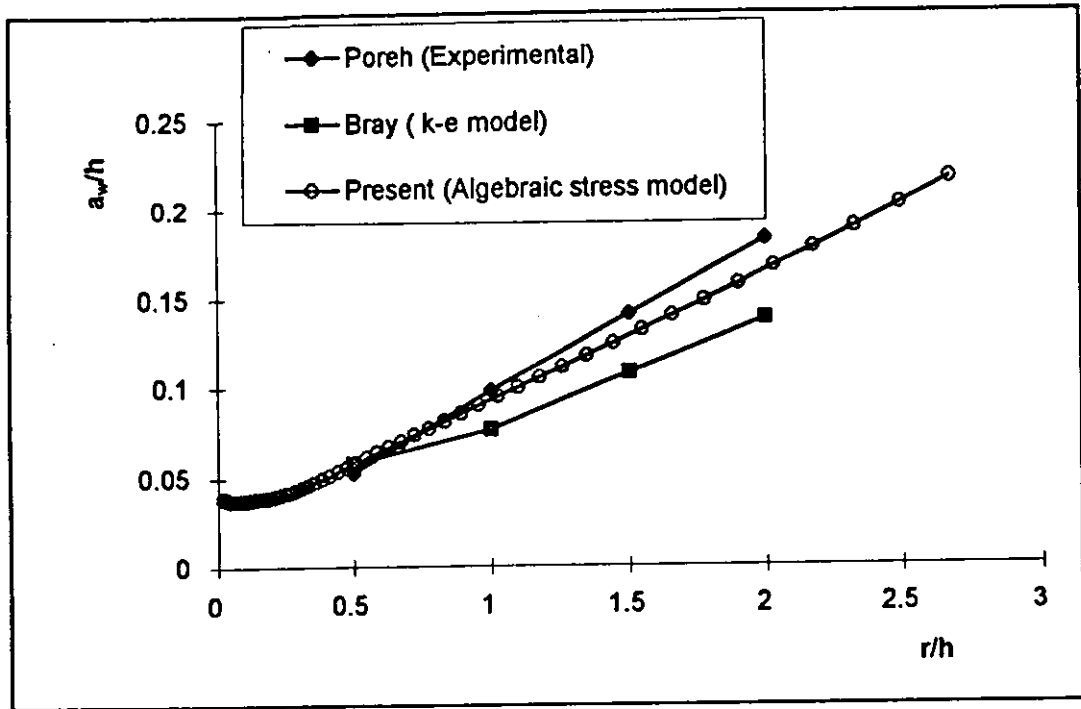


Figure 4.9: Wall jet spreading against r/h for ASM: case 2.

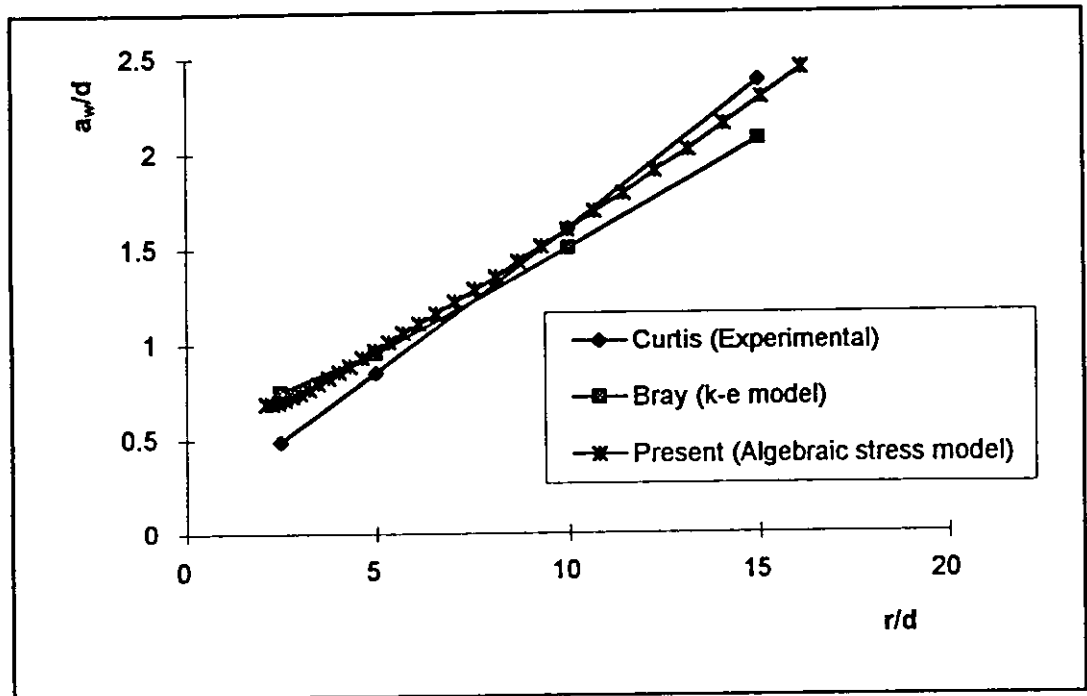


Figure 4.10: Wall jet spreading against r/d for ASM: case 2.

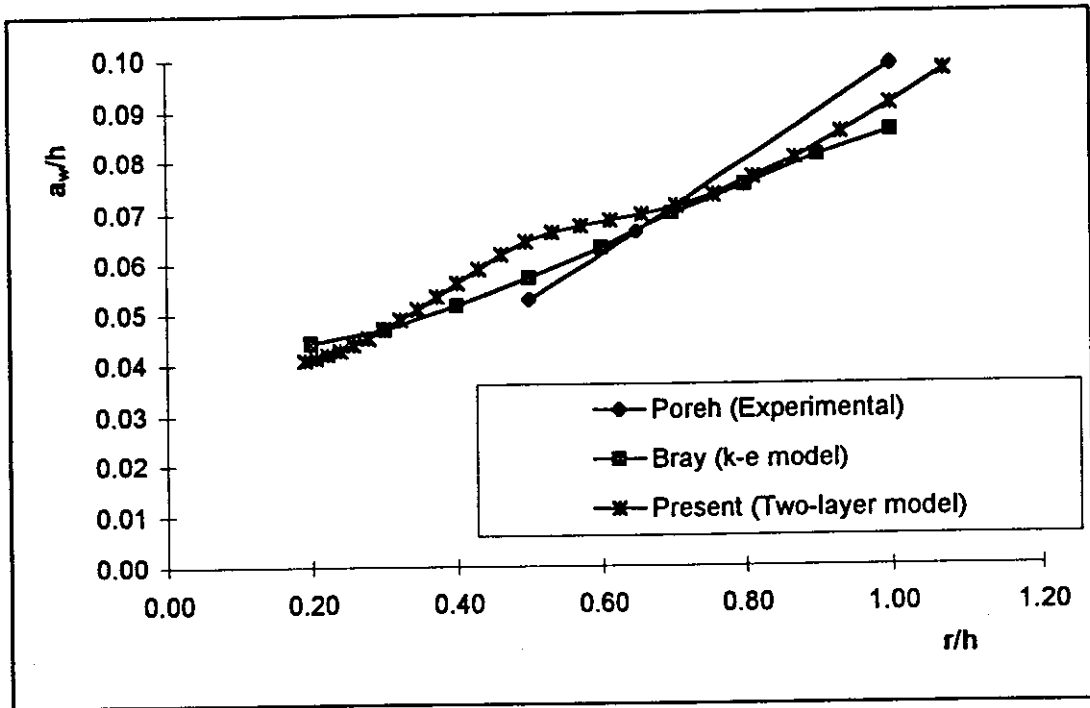


Figure 4.13: Wall jet spreading against r/h for two-layer model: case 1.

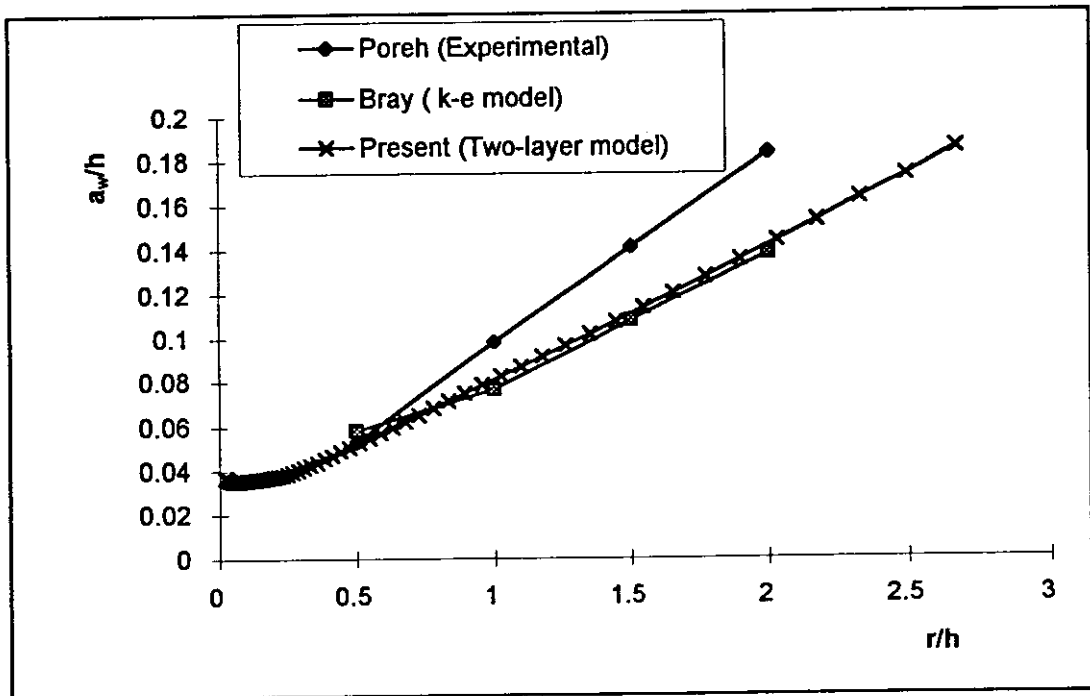


Figure 4.14: Wall jet spreading against r/h for two-layer model: case 2.

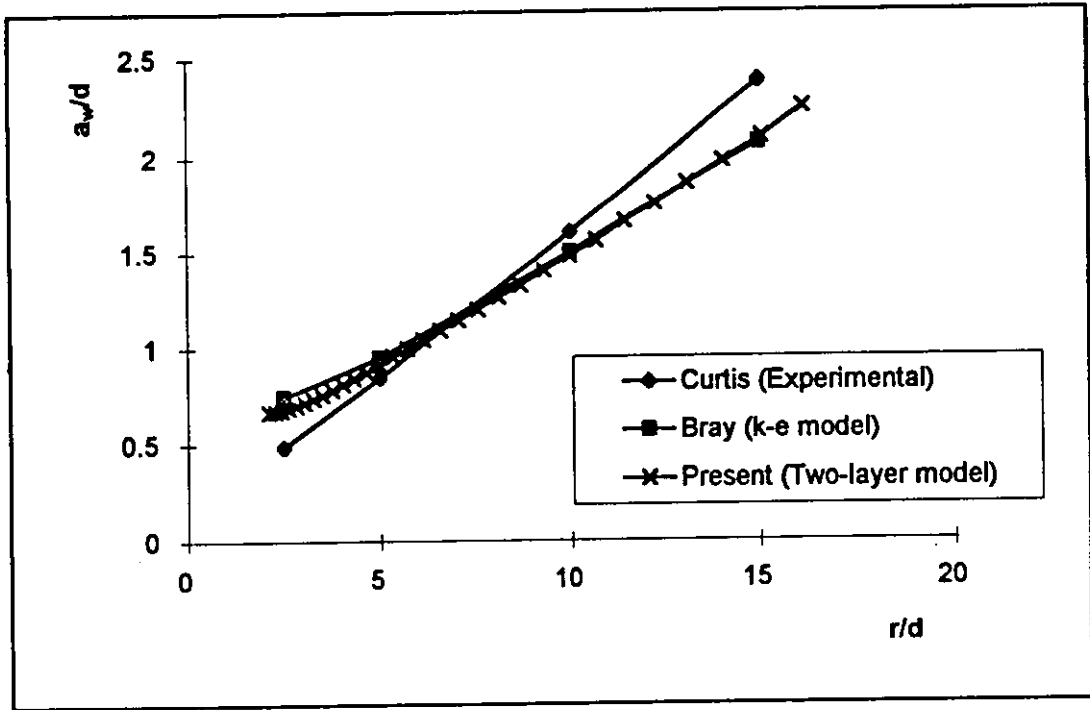


Figure 4.15: Wall jet spreading against r/d for two-layer model: case 2.

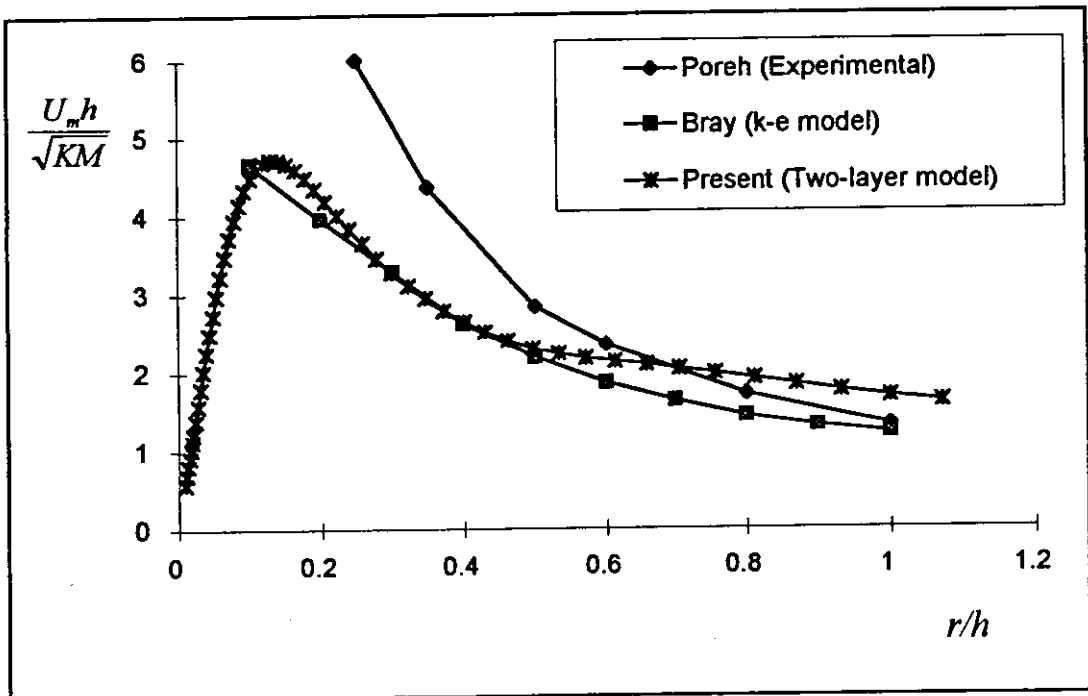


Figure 4.16: Wall jet velocity decay against r/h for two-layer model: case 1.

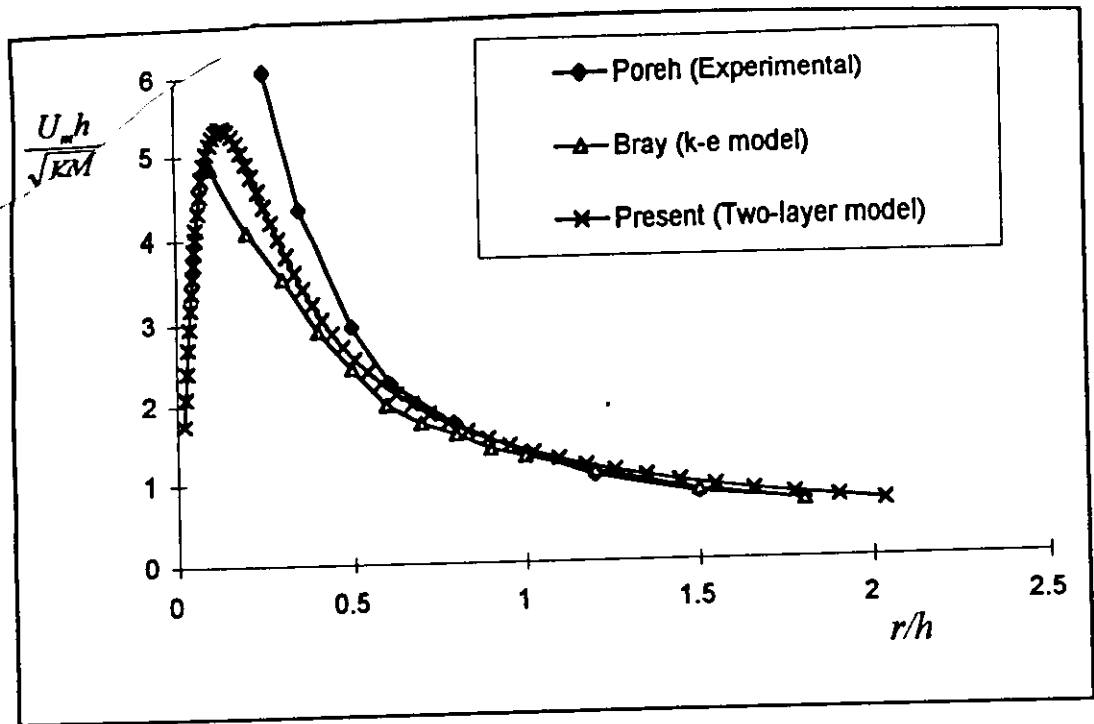


Figure 4.17: Wall jet velocity decay against r/h for two-layer model: case 2.

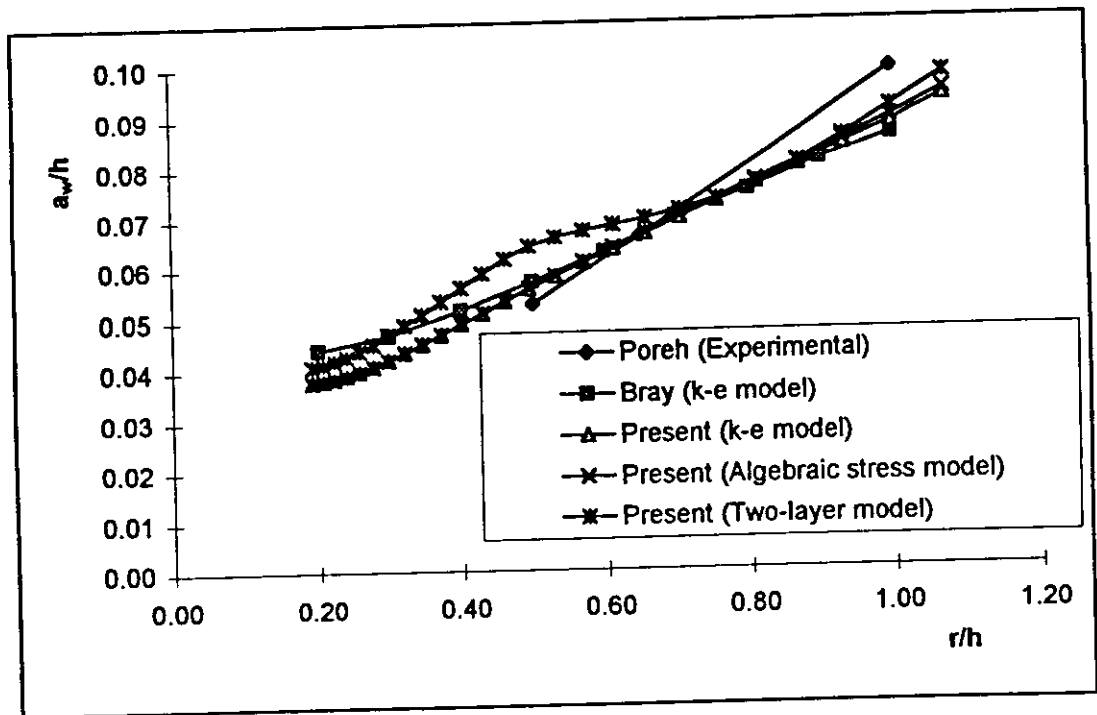


Figure 4.18: Wall jet spreading against r/h for the three models: case 1.

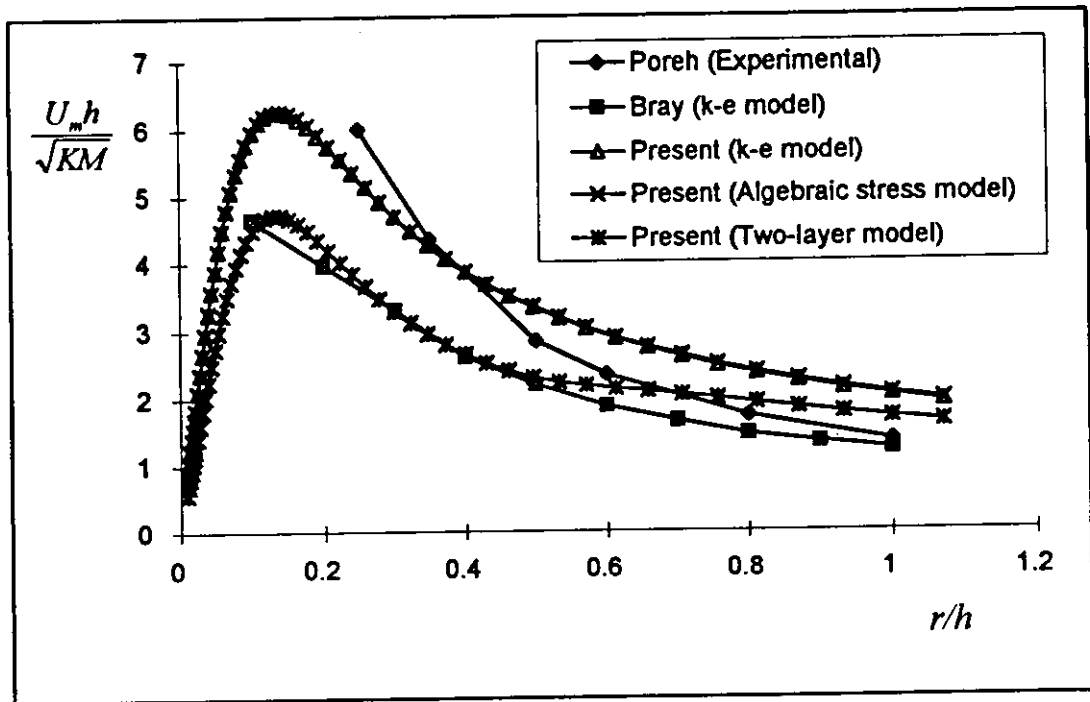


Figure 4.21: Wall jet velocity decay against r/h for the three models: case 1.

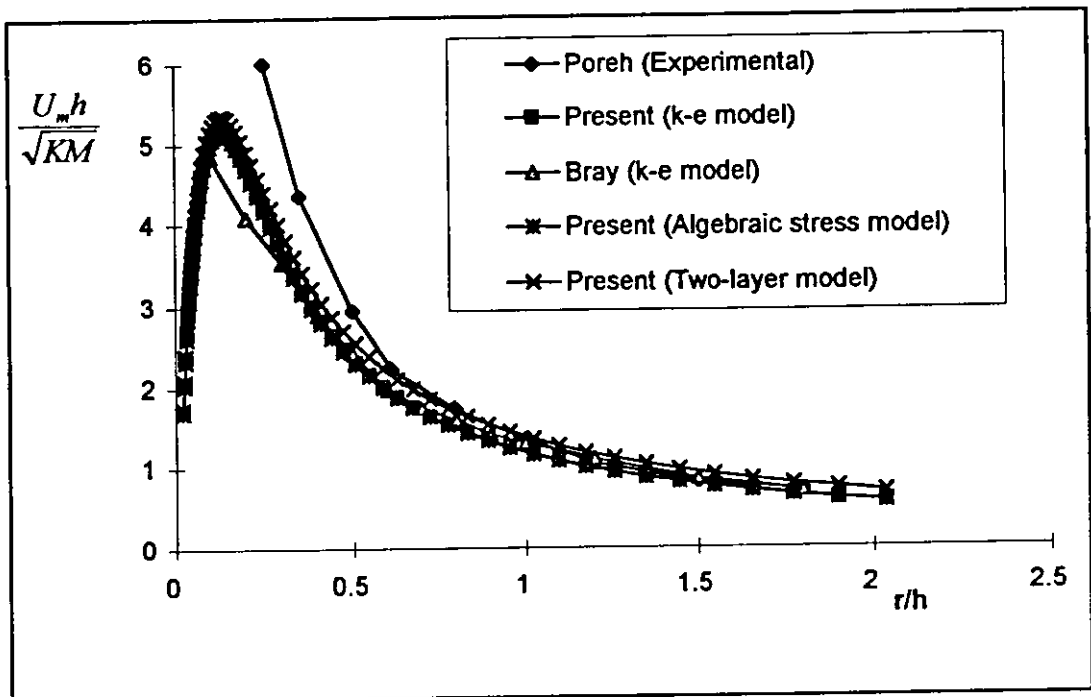


Figure 4.22: Wall jet velocity decay against r/h for the three models: case 2.

Chapter 5

Conclusions and Recommendations

5.1 Introduction

The objective of this thesis was to examine the suitability of three turbulence models for predicting the flow field of axisymmetric impinging jet. The three models are the k - ϵ model, the algebraic stress model, and the two-layer model. The models were tested for two different cases and comparisons with previous experimental and computational results were done. In this chapter, the conclusions and suggestions for further work are summarized.

5.2 Conclusions

The following points are concluded from the present study:

1. The algebraic stress model gives a little better results over the other two models.
2. This improvement does not deserve the additional modeling and computational efforts needed to settle the model.

3. The k- ϵ model results in very good predictions when used with proper grid resolution and mathematical schemes.
4. The two-layer model results were good for the case of fine grid spacing.
5. The grid refinement and distribution are key points in getting good predictions.
6. The multi grid technique was found to be superior in reducing the computational efforts.

5.3 Recommendations

Based on the work conducted in this study, the following points for further work may be suggested :

1. Modeling the full 3-D case is essential since the 2-D modeling has many disadvantages.
2. An important work that must be conducted is to model the flow field inside the nozzle in order to get the proper velocity profile at the nozzle exit.
3. Examining the k- ϵ model with new numerical approaches for this case and more complicated cases (twin jet arrangement, impinging with cross flow, etc.) is needed.

4. Multi grid technique should be used in further numerical work to improve convergence and reduce computational time.
5. Using grid generation to model the real aircraft cases with a body fitted coordinate system may be of importance.
6. Further works should investigate the suitability of the so called multi scale turbulence models.

References

- Abbott, W. A. 1964. Studies of Flow Fields Created by Vertical and Inclined Jets when Stationary or Moving over a Horizontal Surface. Aero. Research Council, CP-911.
- Agarwal, R. K. and Bower, W. W. 1982. Navier-Stokes Computations of Turbulent Compressible Two-Dimensional Impinging Jet Flow Fields. *AIAA Journal*, **26(5)**: 577-584.
- Andersson, H. I. and Nilsen, P. J. 1989. Comparison of Algebraic Reynolds Stress Models for Rotating Flows. *Forum on Turbulent Flows*, **FED-76**: 13-18.
- Araujo, S. R. B., Durao, D. F. G. and Firmino, F. J. C. 1982. Jet Impinging Normally and Obliquely to a Wall. *AGARD*, CP-308.
- Arpaci, V. S. and Larsen, P. S. 1984. *Convection Heat Transfer*. Prentice-Hall, Inc., Englewood Cliffs, New Jersey.
- Baha, M. S. 1994. *Numerical Study of Impinging Jets in Cross-Flow Relevant to Short Take-Off and Vertical Landing Aircraft*. M. Sc. Thesis, Mechanical Engineering Department, University of Jordan.
- Beltaos, S. and Rajaratnam, N. 1974. Impinging Circular Turbulent Jets. *J. of the Hydraulics Division*, American Society of Civil Engineers, **100 (HY10)**: 1313-1328.
- Beltaos, S. and Rajaratnam, N. 1977. Impingement of Axisymmetric Developing Jets. *J. of Hydraulic Research*, **15(4)**: 311-326.
- Borges, A. R. J. and Viegas, D. X. 1982. Interaction of Simple and Multiple Jets with a Plane Surface. *AGARD*, CP-308.

- Bradbury, L. J. S. 1972. The Impact of an Axisymmetric Jet onto a Normal Ground. *Aeronautical quarterly*: 141-147.
- Brady, W. G. and Ludwig, G. 1963. Theoretical and Experimental Studies of Impinging Uniform Jets. *IAS 31st Annual Meeting*, 63-29, New York.
- Bray, D. 1991. *Jets in Cross-Flow and Ground Effects*. Ph.D. Thesis, Cranfield Institute of Technology, RMCS, England.
- Burden, R. L., Faires, J. D. and Reynolds, A. C. 1987. *Numerical Analysis*. Prindle, Webber and Schmidt, Boston, Massachusetts.
- Childs, R. E. 1991. Calculation of Impinging Jet Flows with Reynolds-Stress Models. *29th Aerospace Sciences Meeting*, AIAA-91-0754.
- Childs, E. and Patel, B. 1990. Turbulence Model Performance in V/STOL Flow Field Simulation. *26th Joint Propulsion Conference*, AIAA-90-2248.
- Craft, T. J. and Launder, B. E. 1991. Comparisons of Turbulent Models in a Single Impinging Jet. Proceedings from the UMIST Workshop, *Turbulence Modeling for Impinging Flows*.
- Craft, T. J. and Launder, B. E. 1992. New Wall-Reflection Model Applied to the Turbulent Impinging Jet. *AIAA Journal*, 30(12): 2970-2972.
- Curtis, P. 1986. Jet Research-Quarterly Report no. 1. *BAe MAL*, Kingston, BAe-KAD-N-GEN-3267.
- Curtis, P. 1987. Investigation into the behaviour of a single free jet in free air and impinging perpendicularly on the ground. *BAe MAL*, Kingston, BAe-KAD-R-RES-3349.
- Donaldson, C. D. and Snedeker, R. S. 1971. A Study of Free Jet Impingement. Part 1. Mean Properties of Free and Impinging Jets. *J. of Fluid Mechanics*, 45(2): 281-319.
- Ferziger, J. H.. Simulation of Incompressible Flows. *J. of Computational Physics*, 69(1): 1-48.

- Nosseir, N. S. 1986. Impinging Jets. In: *Encyclopedia of Fluid Mechanics*, 2, Gulf Publication Company.
- Patankar, S. V. 1980. *Numerical Heat Transfer and Fluid Flow*. Hemisphere Publishing Corporation, USA.
- Poreh, M., Tsuei, Y. G. and Cermak, J. E. 1967. Investigation of a Turbulent Radial Wall Jet. *J. of Applied Mechanics*, 89: 457-463.
- Rodi, W. 1976. A New Algebraic Relation for Calculating the Reynolds Stresses. *ZAMM*, 56: T219-T221.
- Rodi, W. 1980. *Turbulence Models and their Applications in Hydraulics - A State of the Art Review*. IAHR, Delft, The Netherlands.
- Rodi, W. 1991. Experience with Two-Layer Models Combining the k-ε Model with a One Equation Model Near the Wall. *29th Aerospace Sciences Meeting*, AIAA-91-0216.
- Sloan, D. G., Smith, P. J. and Smooth, L. D. 1986. Modeling of Swirl in Turbulent Flow Systems. *Eng. Energy Combust. Sci.*, 12: 163-250.
- Smith, A. G., Ing, D. N. and Bailey, P. J. 1990. The Experimental and Computational Study of Jet Impingement Flow Fields with Reference to VSTOL Aircraft Performance. *International Powered Lift Conference*, The Royal Aeronautical Society.
- Zhu, J. 1991. FAST-2D: A Computer Program for Numerical Simulation of Two-Dimensional Incompressible Flows with Complex Boundaries. 690, University of Karlsruhe.

$$G_k = \frac{\sigma}{\rho} - \left[(uu)_d \left(\frac{\partial U}{\partial x} \right) + (uv)_d \left(\frac{\partial U}{\partial r} + \frac{\partial V}{\partial x} \right) + (vv)_d \left(\frac{\partial V}{\partial r} \right) \right] , \quad (\text{A.4})$$

$$\bar{P}_x = \frac{\mu_t}{\rho} \left[4 \left(\frac{\partial U}{\partial x} \right)^2 + 2 \left(\frac{\partial U}{\partial r} \right)^2 + 2 \left(\frac{\partial U}{\partial r} \right) \left(\frac{\partial V}{\partial x} \right) \right] , \quad (\text{A.5})$$

$$\bar{P}_r = \frac{\mu_t}{\rho} \left[4 \left(\frac{\partial V}{\partial r} \right)^2 + 2 \left(\frac{\partial V}{\partial x} \right)^2 + 2 \left(\frac{\partial U}{\partial r} \right) \left(\frac{\partial V}{\partial x} \right) \right] , \quad (\text{A.6})$$

$$\bar{P}_{xr} = \frac{\mu_t}{\rho} \left[2 \left(\frac{\partial U}{\partial r} \right) \left(\frac{\partial V}{\partial r} \right) + \left(\frac{\partial U}{\partial r} + \frac{\partial V}{\partial x} \right) \left(\frac{\partial U}{\partial x} + \frac{\partial V}{\partial r} \right) + 2 \left(\frac{\partial U}{\partial x} \right) \left(\frac{\partial V}{\partial x} \right) \right] , \quad (\text{A.7})$$

476770

$$\tilde{P}_{xx} = - \left[2(\overline{uu})_d \left(\frac{\partial U}{\partial x} \right) + 2(\overline{uv})_d \left(\frac{\partial U}{\partial r} \right) \right] \quad , \quad (\text{A.8})$$

$$\tilde{P}_{rr} = - \left[2(\overline{vv})_d \left(\frac{\partial V}{\partial r} \right) + 2(\overline{uv})_d \left(\frac{\partial V}{\partial x} \right) \right] \quad , \quad (\text{A.9})$$

$$\tilde{P}_{xr} = - \left[(\overline{uu})_d \left(\frac{\partial V}{\partial x} \right) + (\overline{uv})_d \left(\frac{\partial V}{\partial r} + \frac{\partial U}{\partial x} \right) + (\overline{vv})_d \left(\frac{\partial U}{\partial r} \right) \right] \quad , \quad (\text{A.10})$$

and G is the production of turbulent energy defined in the k - ϵ model by

$$G = \mu_t \left\{ 2 \left[\left(\frac{\partial U}{\partial x} \right)^2 + \left(\frac{\partial V}{\partial r} \right)^2 + \left(\frac{V}{r} \right)^2 \right] + \left(\frac{\partial U}{\partial r} + \frac{\partial V}{\partial x} \right) \right\} .$$